Expanding the family of mineral-like anhydrous alkali copper sulfate framework structures: New phases, topological analysis and evaluation of ion migration potentialities

Artem S. Borisov[1], Oleg I. Siidra[1,2*], Vadim M. Kovrugin[3#], Andrey A. Golov[4], Wulf Depmeier[5], Evgeny V. Nazarchuk[1], Astrid Holzheid[5]

[1] Department of Crystallography, St. Petersburg State University, University Embankment 7/9, 199034 St. Petersburg, Russia

[2] Kola Science Center, Russian Academy of Sciences, Apatity 184200, Murmansk Region, Russia

[3] ICMCB-CNRS, Université de Bordeaux, Bordeaux INP, UMR 5026, 33600 Pessac Cedex, France

[4] Centro de Investigación Cooperativa de Energías Alternativas (CIC energiGUNE), Basque Research and Technology Alliance (BRTA), Parque Tecnológico de Alava, 01510 Vitoria-Gasteiz, Spain

[5] Institut für Geowissenschaften der Universität Kiel, Olshausenstr. 40, D-24098 Kiel, Germany

*o.siidra@spbu.ru

#kovrugin_vm@hotmail.com

Abstract Two novel compounds, $K_2Cu_3(SO_4)_4$ and $KNaCu(SO_4)_2$, were synthesized. The crystal structure of $K_2Cu_3(SO_4)_4$ is based on a $[Cu_3(SO_4)_4]^{2-}$ framework with relatively simple bond topology, but with four different CuO_n polyhedron geometries. The K^+ cations reside in the pores of the framework. The $[Cu(SO_4)_2]^{2-}$ framework in $KNaCu(SO_4)_2$ encloses large elliptical channels running along [001]. Larger channels are occupied by K^+, whereas smaller ones are filled by Na^+. The BVEL (bond valence energy landscape) approach demonstrated to be a useful method for the prediction of the mobility of alkali metal ions in various structures. By means of this approach, the threshold energies at which isosurfaces begin to percolate as well as the directions of possible ion migration in the structures were determined. The modelling of ion migration maps by the analysis of procrystal electron density distribution was used to rapidly identify ion migration pathways and limiting barriers between particular crystallographic sites in the structures under consideration. Its consistency and complementarity with the BVEL method have been demonstrated. Both approaches revealed a relatively low ion threshold percolation and migration barriers in the cryptochalcite-type structures (cryptochalcite: $K_2[Cu_5O(SO_4)_5]$). Hence, one may assume that its 3D framework type is suited for ion transport applications. The performed review of all known members of the groups of anhydrous copper sulfates did not reveal a correlation between the porosity of the framework structures and a manifestation of ion conduction properties.

Keywords: sulfates, copper, framework structures, bond-valence energy landscape, procrystal electron density distribution, electrochemistry

1. Introduction

Anhydrous sulfates represent an actively studied field in solid-state chemistry. There are several reasons for that, but a particularly interesting one - at least for material scientists - is the quest for novel electrode materials for possible application as cathodes in rechargeable metal-ion batteries (Goodenough & Park, 2013; Masquelier & Croguennec, 2013; Sun *et al*., 2019).

Currently, the most commonly used cathode polyanionic materials are phosphate based, but sulfates seem to present a promising alternative given their superior electronegativity (Lander *et al*., 2018; Barpanda, 2015; Rousse & Tarascon, 2014). With regard to the cations lithium-ion based batteries dominate the current energy storage market, but sodium and potassium are believed to be potentially good substitutes for lithium because of their high chemical activity, their superior safety aspects and lower costs, while keeping the energy density on an acceptable level. Furthermore, because of the boosting demand for Li-ion batteries in the fields of e.g. electric vehicles, mobile communication devices or cordless tools, and not least because economic Li resources are limited in number and the deposits are concentrated in only a few countries, the Li supply is likely to become critical in the medium to long term. Unlike Li, K and Na resources are abundant and available throughout the world, which makes them uncritical and low cost raw materials even in the long run. This is why sodium-and potassium-ion batteries are considered to be prospective alternatives to the currently prevailing lithium-ion based technology (Hwang *et al*., 2017; Hosaka *et al*., 2020). It goes without saying that plenty of scientific and technical problems have to be solved, e.g. in the fields of crystallography, crystal chemistry and materials sciences, before any widespread real life applications could even be taken into serious consideration.

As far as we are aware of, copper-based compounds have only rarely been considered as materials for advanced battery electrodes owing to the low operating voltages of the Cu^{+}/Cu^{2+} redox couple and also because of their instability upon electrochemical cycling. Nevertheless, Xu *et al.* (2014) demonstrated reversible electrochemical activity in layered copper oxide materials based on the Cu^{2+}/Cu^{3+} redox couple with its high operating voltage of ~ 4 V vs Na . Further studies demonstrated that certain complex Cu-based compounds with relatively stable structures might also be considered as potential electrode materials, at least in principle. Examples are the disordered wurtzite-type structure of Li_2CuVO_4 (Ben Yahia *et al*., 2016) and $Li_2Cu_2O(SO_4)_2$ (Sun *et al*., 2015) the structure of which is based on copper sulfate chains. Unfortunately, neither of them survives electrochemical delithiation because the Li^{+} cations are essential for their statics,

which means that their removal during cycling results in deformation and subsequent collapse of the structure. This observation lends itself to a hypothesis that Cu-based 3*D* framework structures where cations, such as Li^+, Na^+ or K^+ , are not an integral part of the framework but act as exchangeable guest species might provide good long-term structural stability upon electrochemical cycling. In line with this idea we herein contribute to an enhanced exploration of alkali copper sulfate compounds with stable framework architecture. We report on the synthesis and crystal structures of two new anhydrous alkali cations containing framework compounds of composition $K_2Cu_3(SO_4)_4$ and $KNaCu(SO_4)_2$. Notably, the crystal structure of the latter exhibits high porosity and the K and Na cations are completely segregated.

It should be noted that the synthesis of both compounds was inspired by lessons learned from Nature, since both stoichiometries, as well as related ones, were known from the investigation of anhydrous fumarolic sulfate minerals. Recently, similar "from minerals to materials" approaches proved effective for several electrochemical applications. One of the examples is the mineral eldfellite, ideally $NaFe^{3+}(SO_4)_2$, which was discovered in the fumaroles of Eldfell volcano (Balić-Žunić *et al*., 2009). Analogues of eldfellite, synthesized later (Singh *et al*., 2015; Yu *et al*., 2017; Ri *et al*., 2018), were shown to present highly stable electrochemical cycling behavior in a Na half-cell. Another example of a mineral serving as a basis for the investigation of intercalation properties is langbeinite, $K_2Mg_2(SO_4)_3$. An impressive number of synthetic langbeinite-type compounds with various combinations of elements is known (*e.g.* Lander *et al*., 2017; Trussov *et al*., 2019).

Over the past few years (Siidra *et al*., 2017, 2018*a*,*b*,*c*, 2019*b*,*c*, 2020*a*,*b*), we have been actively investigating fumarolic mineral associations from the scoria cones of the Tolbachik volcano (Kamchatka Peninsula, Russia). Several of the sulfate minerals which grow abundantly in the alteration zones of active fumaroles have attracted attention also from the viewpoint of electrochemistry, for instance kröhnkite $Na_2Cu(SO_4)_2{\cdot}2H_2O$ (Barpanda *et al*., 2014; Watcharatharapong *et al*., 2017) and blödite $Na_2Mg(SO_4)_2{\cdot}4H_2O$ (Reynaud *et al*., 2014). We have

also undertaken several studies aimed at the understanding of cyclic hydration/dehydration processes of anhydrous sulfate minerals (Siidra *et al*., 2018*a*, 2019*a*), and studied the influence of these processes on the electrochemical properties of the synthetic analogue of saranchinaite $Na_2Cu(SO_4)_2$ (Kovrugin *et al*., 2019). As an aside we note that anhydrous sulfate minerals of alkali and transition metals are extremely unstable when exposed to air, which considerably complicates their experimental investigation.

The novel compounds described in this work have distantly related mineral analogues also discovered earlier on the Tolbachik volcano. $K_2Cu_3(SO_4)_4$ has general $A^+_2M^{2+}_3(SO_4)_4$ stoichiometry, which was first observed for itelmenite, $Na_2CuMg_2(SO_4)_4$ (Nazarchuk *et al*., 2018), and $KNaCu(SO_4)_2$ is a K-Na stoichiometric analogue of saranchinaite $Na_2Cu(SO_4)_2$ (Siidra *et al*., 2018*a*).

In addition to the discussion of the new compounds, an overview of the different topologies of all currently known - synthetic and natural - porous anhydrous framework sulfates of copper and alkali metals is presented, complemented by an evaluation of possible Na^+ and K^+ migration pathways within their frameworks employing the BVEL method as well as an analysis of the procrystal electron density distribution.

2. Experimental

2.1 Synthesis of new compounds

2.1.1 Synthesis of $K_2Cu_3(SO_4)_4$

$K_2Cu_3(SO_4)_4$ was prepared by the chemical vapor transport (CVT) technique (e.g. Binnewies *et al*., 2013). A mixture of KCl (Aldrich ≥99.0%, 0.149 g, 2 mmol), $CuSO_4$ (Aldrich ≥99.0%, 1.596 g, 4 mmol), CuO (Aldrich ≥99.0%, 0.239 g, 3 mmol) and NaCl (Aldrich ≥99.0%, 0.175 g, 3 mmol) was ground and loaded into a silica ampoule (ca. 15 cm), which was evacuated to 10^{-2} mbar and sealed. Reactants were predried at 100 °C for 2 h. The ampoule was placed in a tube furnace and heated. After 5 hours, a temperature of 600°C was reached, and held for 48 h.

The furnace was cooled to room temperature at a rate of 7°C/min. The product in the "cold zone" of a tube consisted of blue crystals of $K_2Cu_3(SO_4)_4$ in association with green crystals of the synthetic analogue of fedotovite, $K_2Cu_3O(SO_4)_3$ (Starova *et al.*, 1991) (Fig. 1*a*). The as-prepared $K_2Cu_3(SO_4)_4$ is moisture-sensitive and starts to hydrate after one week of exposure to air.

2.1.2 Synthesis of $KNaCu(SO_4)_2$

$KNaCu(SO_4)_2$ was obtained under high-pressure/high-temperature (HP/HT) conditions. The synthesis was performed using the piston cylinder module of a Voggenreiter LP 1000-540/50 system installed at the Institute of Geosciences, University of Kiel. KCl (Aldrich ≥99.0%, 0.149 g, 2 mmol), $CuSO_4$ (Aldrich ≥99.0%, 0.798 g, 2 mmol) and Na_2SO_4 (Aldrich ≥99.0%, 0.142 g, 1 mmol) were weighed, mixed, and finely ground. The mixture was placed into a platinum capsule (outer diameter = 3 mm, wall thickness = 0.2 mm, length = 12 mm). The capsule was sealed on both sides and placed into the center of a 1/2-inch piston cylinder talc−Pyrex assembly. The pressure increased for 5 minutes at a rate of 0.2 GPa/min, until a working pressure of 1 GPa was reached, whereupon the temperature program was started at a rate of 60°C/min up to the operating temperature of 600°C which was maintained at the set pressure for 6 hours. The cooling time was 10 h (cooling rate ≈ 60°C/h). Simultaneously with cooling, the pressure was released at a rate of 0.1 GPa/h. After room temperature had been reached, the experiment was decompressed during 20 min. The capsule was extracted from the high-pressure assembly and cut for further investigations. The product consisted of light blue transparent $KNaCu(SO_4)_2$ crystals in association with milky white crystals of Na_2SO_4 and small yellow crystals of $K_2(PtCl_6)$ (as product of a reaction with the Pt capsule (Fig. 1*b*)).

2.2 X-ray experiment

The crystals of $K_2Cu_3(SO_4)_4$ and $KNaCu(SO_4)_2$ were examined under an optical microscope and suitable ones selected and mounted on glass fibers for the data collection. The

single crystal X-ray data collection was carried out using a Bruker «Kappa APEX II DUO» diffractometer with a micro-focus X-ray tube (Mo*K*α radiation) operating at 50 kV and 0.6 mA. For each crystal more than a hemisphere of data was collected with a frame width of 0.5° in ω, and 10 s counting time spent for each frame. The data were integrated and corrected for absorption using a multi-scan type model using the Bruker programs APEX (Bruker, 2014). The structures were solved by direct methods. $K_2Cu_3(SO_4)_4$ is monoclinic, space group *C*2/*c* (no. 15), *a* = 13.6088(5) Å, *b* = 11.9627(5) Å, *c* = 17.0791(7) Å, β = 112.450(1)°, *V* = 2569.7(2) Å^3, R_1 = 0.023 (Table 1). $KNaCu(SO_4)_2$ is also monoclinic, *C*2/*c*, *a* = 15.972(1) Å, *b* = 9.4576(6) Å, *c* = 9.0679(6) Å, β = 93.635(1)°, *V* = 1367.0(2) Å^3, R_1 = 0.029. Both structures were refined using the SHELX software package (Sheldrick, 2015). All the atoms were refined with anisotropic atomic displacement parameters, no conspicuous anomalies were observed.

3. Results

3.1 Cation coordination

3.1.1 $K_2Cu_3(SO_4)_4$

The crystal structure of $K_2Cu_3(SO_4)_4$ contains four symmetrically independent Cu sites with different coordination environments (Fig. 2, Table 4). Cu2 and Cu4 are in special positions (Wyckoff letters and site symmetry 4*a* -1 and 4*e* 2, respectively) and impose their symmetry on the respective coordination polyhedra. Cu1 and Cu2 are coordinated by six oxygen atoms forming CuO_6 octahedra, which are differently distorted due to the Jahn-Teller effect and by symmetry. Six-fold coordination is common for oxysalts of divalent copper in general, and among Cu^{2+} sulfates in particular (Burns & Hawthorne, 1995). The average <Cu–O> distances are 2.095 Å and 2.108 Å for Cu1 and Cu2, respectively. The $\Delta_{oct}\times10^3$ octahedral distortion values (Brown & Shannon, 1973, Wildner, 1992) are 4.21 and 7.07 for the $Cu1O_6$ and $Cu2O_6$, respectively. These values reflect the fact that the coordination polyhedron around Cu2 is more distorted than that around Cu1, despite its higher local symmetry. The Cu1O6 polyhedron may be regarded as

intermediate between a perfect (4+2) coordination where the distances to the apical O atoms are nearly equal, and a (4+1+1) coordination where they are markedly different. The difference between the two elongated Cu1-O bonds amounts to about 10% and thus are close to 12.5% suggested earlier as a borderline between (4+2) and (4+1+1) coordinations (Burns & Hawthorne, 1995). Note that the shorter of the elongated bond (Cu1 - O15, 2.126 (2) Å) is not much different from the average Cu1-O_{eq} (2.022 Å) (O_{eq} = O atoms in the equatorial "plane"). The Cu2O6 polyhedron is a (4+2) distorted, centrosymmetric, elongated octahedron. The Cu3 atom is coordinated by five oxygens, four of which are in the equatorial plane, and one (O13) occupies the apical vertex, thus in good approximation it forms a distorted (4+1) CuO_5 square pyramid with average <Cu3–O> distance 2.017 Å. An additional sixth O atom (O9) opposite to O13 completes a quasi-(4+1+1) octahedral geometry, however its distance of 3.022(2) Å from Cu3 can only be qualified as a very weak bond. This bond is 33% longer than the opposite elongated bond to O13 (2.270(2) Å). In a first approximation, Cu4 has square planar coordination with four equatorial oxygen atoms (Fig. 4). The square is complemented by two additional long Cu-O bonds of 2.843(2) Å to the apical oxygens thus resulting in a strongly distorted CuO_{4+2} octahedron. This polyhedron has point symmetry 2, and the equatorial "plane" is better characterized as a flattened disphenoid.

The four S^{6+} sites in the asymmetric unit form fairly regular SO_4 tetrahedra. The average bond lengths span the narrow range 1.470 -1.476 Å and are in excellent agreement with average <S-O> distance of 1.473 Å reported for sulfate minerals by Hawthorne *et al.* (2000).

For the two symmetrically independent K sites all of the K-O bonds ≤ 3.55Å were taken into account. Eleven O atoms coordinate the K1 atom, and ten oxygens are bonded to K2. Both coordination environments are common for K^+ cations (Waroquiers *et al.*, 2017). The Bond Valence Sums (BVS) for both K sites are slightly above the nominal 1 *v.u.* (valence units) (1.08

and 1.01 *v.u.* for K1 and K2, respectively, Table 6), which may indicate strong chemical bonding and thus localization.

3.1.2 $KNaCu(SO_4)_2$

The crystal structure of $KNaCu(SO_4)_2$ contains one symmetrically independent Cu site, two S sites, one K and two Na sites (Fig. 3, Table 5). Cu, S, and K are in general positions, Na1 and Na2 in special positions (Wyckoff letters and site symmetries 4*c* -1 and 4*e* 2, respectively).

The S atoms form approximately regular SO_4 tetrahedra, both with respect to the S-O bond length and to the O-S-O angles (Table 5). The tetrahedra can be considered as essentially rigid bodies.

Four Cu-O bonds with distances around 2 Å form a nearly square planar configuration, the bond with a fifth O atom (O7) is longer (about 2.2 Å) and its bond is oriented approximately perpendicular to the square plane. The latter atom can thus be considered to be apical. In first approximation the Cu coordination can thus be considered to be of the (4+1) type. However, there is an additional close O8 atom on the opposite side of the plane. It has a significantly longer distance from Cu than the opposite O7, but still contributes weakly to the BVS (Fig. 3, Tables 5 and 7). Furthermore, the Cu1-O8 bond is strongly bent away from the 180 degrees which would be expected for an ideal (4+1+1) octahedron. The bending is towards the O1 atom such that the angle O8-Cu1-O1 reduces from ideally 90 to 61.46(9) degrees. Note that O1 and O8 belong to the same SO_4 tetrahedron where they form an edge. Consequently, they also form an edge of the CuO_6 polyhedron just described (Fig. 3, see also below).

The crystal structure refinement yielded the important, yet not unexpected, result that K^+ and Na^+ cations are completely segregated and do not substitute for each other. The potassium atom forms a KO_{11} polyhedron with an average <K–O> distance of 3.01 Å, and both Na atoms have octahedral coordination environments with different degree of distortion. The average <Na–O> distances are 2.501 Å and 2.421 Å for Na1 and Na2, respectively. The BVS for K1, Na1, and Na2 are respectively 1.09, 0.88, and 1.10 *v.u.* The value of 0.88 indicates that Na1 is under-bonded

lending itself to a speculation that this might be related with a possible delocalization of Na1 and perhaps participation in ion migration processes (but see below).

3.2. Description of the crystal structures

3.2.1 $K_2Cu_3(SO_4)_4$

The crystal structure of $K_2Cu_3(SO_4)_4$ is based on a $[Cu_3(SO_4)_4]^{2-}$ framework (Fig. 4*a*,*b*) with relatively simple bond topology. Each CuO_n (n = 4-6) polyhedron shares all of its corners with SO_4 tetrahedra. In turn, each SO_4 tetrahedron shares three oxygens with Cu centered polyhedra and one with K. Nominally, the framework can be decomposed into zigzag layers as shown in Fig. 4*b*,*c*. In turn, the layers consist of porous bands (Fig. 4*d*,*e*) running along the *a* axis. The K^+ cations reside in the pores of the $[Cu_3(SO_4)_4]^{2-}$ framework.

3.2.2 $KNaCu(SO_4)_2$

Each SO_4 tetrahedron shares one of its O atoms (O2 or O6, respectively) exclusively with K and Na, the remaining three are connected with Cu. The Cu polyhedron shares corners with five SO_4 tetrahedra (two centered by S2 and three by S1) corresponding to the (4+1) configuration mentioned above. As mentioned before, O8 with its long distance and O1 in the equatorial plane belong to the same tetrahedron around S2, together they form one of its edges. Therefore, this situation can be regarded as edge-sharing between the SO_4 tetrahedron and the CuO_6 octahedron. As a consequence, this configuration is of course not the usual (4+1+1) type, but could be symbolized as ((4+1)+1).

Edge-sharing of CuO_6 polyhedra with SO_4 tetrahedra is all but common (Hawthorne *et al.*, 2000), probably because of unfavourable repulsive interactions between the cations. For $KNaCu(SO_4)_2$ the Cu1-S2 distance along the S2-O8-Cu1 connection is only 2.81 Å, compared to the considerably longer distances along connections via corner-sharing O atoms, e.g. around 3.2 Å for S1-O-Cu. Edge-sharing between CuO_6 octahedra and SO_4 tetrahedra has also been reported

for the crystal structure of chlorothionite, $CuK_2Cl_2SO_4$. (Giacovazzo *et al*., 1976) with an even shorter Cu-S distance of 2.59 Å. Overall, this type of connection between Cu^{2+} octahedra and $(SO_4)^{2-}$ is extremely rare in minerals and oxysalts of divalent copper (Hawthorne *et al*., 2000).

Together with SO_4 tetrahedra the CuO_6 polyhedra form the porous $[Cu(SO_4)_2]^{2-}$ framework shown in projection in Fig. 5*a*,*b*. It contains two types of channels running along the *c* axis (Fig. 5*a*,*d*). The larger elliptical channels are occupied by K^+, whereas the smaller ones are filled by Na^+ represented by Na2 sites. Na^+ cations in the Na1 sites reside at inversion centers in smaller cavities shown in Fig. 5*d*.

3.3 Topological analysis of anhydrous Cu-SO_4 frameworks.

In the following we present an analysis and comparison of all the topologies occurring in anhydrous framework copper sulfates known to date. This is deemed useful as such an approach might facilitate an evaluation of their potentialities as ion exchange materials. Only those synthetic compounds and natural minerals will be included which have 3D framework structures formed by corner and/or edge sharing of CuO_n polyhedra and SO_4 groups. Some cases of other cations substituting for divalent copper, or where additional positions are occupied by other metals, have also been included. The former case is realized in the mineral glikinite, with the ideal end formula $Zn_3O(SO_4)_2$ (Nazarchuk *et al*., 2020), where in all three symmetrically independent atomic sites there is a significant amount of Cu^{2+} substituting for Zn, the overall Zn:Cu ratio is approximately 2:1 and the formula is $(Zn,Cu)_3O(SO_4)_2$. The latter case is realized by itelmenite $Na_2CuMg_2(SO_4)_4$ (Nazarchuk *et al*., 2018). Note that the majority of the compounds, satisfying the mentioned criteria, occur naturally as minerals. For only a few listed synthetic compounds no mineral counterpart is known, at least up to date (Table 8 and 9). The considered cases are subdivided into two groups. The first one contains the cases with empty framework cavities (Table 8). Here one finds the simple copper sulfate $Cu(SO_4)$, also known as mineral chalcocyanite (Wildner & Giester, 1988; Siidra *et al*., 2018b), the double sulfate of copper and zinc hermannjahnite $CuZn(SO_4)_2$

(Siidra *et al*., 2018b), unknown yet as synthetic compound, and also the isostructural dravertite $CuMg(SO_4)_2$ (Pekov *et al*., 2017), as well as two oxysulfates with additional oxygen atoms in the structure (Krivovichev *et al*., 2013), viz. dolerophanite $Cu_2O(SO_4)$ (Effenberger, 1985) and glikinite $(Zn,Cu)_3O(SO_4)_2$ (Nazarchuk *et al*., 2020). In the second group of compounds (Table 9) alkali metal cations fill cavities and/or channels in the framework (highlighted by square brackets in the formulas below). This group includes the recently discovered minerals saranchinaite $Na_2[Cu(SO_4)_2]$ (Siidra *et al*., 2018*a*), cesiodymite $CsK[Cu_5O(SO_4)_5]$ (Pekov *et al*., 2018) and the isostructural cryptochalcite $K_2[Cu_5O(SO_4)_5]$ (Pekov *et al*., 2018), as well as itelmenite $Na_2[CuMg_2(SO_4)_4]$ (Nazarchuk *et al*., 2018). Another listed sulfate mineral - kamchatkite $K[Cu_3O(SO_4)_2]Cl$ (Siidra *et al*., 2017) contains additional KCl complexes in the cavities of the framework.

The topological classification was carried out using the ToposPro program package (Blatov *et al*., 2014). For all considered structures, the values for the framework porosity (FP) were calculated by means of ToposPro, employing Slater atomic radii, and compared with the framework density (FD), calculated as the number of framework forming cations (Cu/Zn/Mg and S) per 1000 $Å^3$. The separation of the Cu-SO_4 frameworks into two groups (Table 8 and 9) correlates well with the calculated values of FP and FD. The crystal structures of hermannjahnite, chalcocyanite, glikinite and dolerophanite are characterized by relatively high FD values (Table 8), with dolerophanite having the densest framework. It is interesting to note that the presence of an additional oxygen atom in the structures of glikinite and dolerophanite - which allows to segregate copper atoms into tetrahedral anion-centered OCu_4 complexes - makes them denser than the structures without this crystal chemical feature. The group of copper sulfates with alkali cations (Table 9) contains structures with significantly higher porosity and concomitantly lower density. Itelmenite (FD = 23.19) has the densest framework in this group. Interestingly, kamchatkite, cryptochalcite and the isostructural cesiodymite have very similar values of FD and FP. Note, again, the presence of additional oxygen atoms in the structures of these three minerals. The new

framework type of $K_2[Cu_3(SO_4)_4]$ described in this paper has an intermediate value FD = 21.79. The new $KNaCu(SO_4)_2$ sulfate also described in this work, as well as the related $K_2Cu(SO_4)_2$ (Zhou *et al.*, 2020), have the highest porosity among all considered framework anhydrous copper sulfates. Saranchinaite $Na_2Cu(SO_4)_2$ (Siidra *et al.*, 2018*a*) and its synthetic analogue (Kovrugin *et al.*, 2019) have the same cation to anion ratio as $KNaCu(SO_4)_2$ and $K_2Cu(SO_4)_2$, but their structural architectures are completely different and the framework topologies unrelated, yet their FP values coincide. As one would have expected, FD decreases in the series of $A_2Cu(SO_4)_2$ compounds with increasing ionic radii of the A^+ and concurrent increase of the unit-cell volume. Analysis of the porosities of $A_2Cu(SO_4)_2$ compounds shows that the FD characteristic is more sensitive than FP and better reflects all structural features.

In order to find similar topological patterns among the structures, the standard simplification method was applied (Blatov *et al.*, 2014). The procedure includes contracting polyatomic building units (e.g. octahedra or tetrahedra) to their centroids, thus forming nodes, and removing 0-, 1- and 2-coordinated nodes (Fig. 6). The resulting simplified nets were compared with the known nets from the ToposPro topological database (TTD). In addition, the intra-frameworks cages of the new $K_2Cu_3(SO_4)_4$ and $KNaCu(SO_4)_2$ structures were characterized by the natural tiling partition (Blatov *et al.*, 2007). According to the results of the topological analysis, the structure of the new $K_2Cu_3(SO_4)_4$ in the standard representation has an 8-nodal 4-, 5-, 6-coordinated net, which was unknown in other structures (Fig. 7). The total point symbol (Blatov *et al.*, 2010) of the net is $\{4.6^5\}\{4^2.6^4\}_2\{4^3.6^6.8\}_2\{4^4.6^2\}_6\{4^6.6^6.8^3\}\{4^6.6^7.8^2\}_2$. The natural tiling consists of $[4^3]$, $[4.6^2]$, $[4^7.6^8]$, and $[4^8.6^8]$ tiles in a 5:4:1:1 ratio (Fig. 7). Thus, the framework has four types of cages. Only the latter two tiles are spacious enough to accommodate potassium atoms. These cages are connected to each other through 6-membered rings and form 3-periodic channel system with **pts** topology (Fig. 8*a*). The widest channels have zigzag shape and run along the *c* axis. The **pts** topology is known from the crystal structure of cooperite PtS (Rozhdestvina *et al.*, 2016).

The underlying net of $KNaCu(SO_4)_2$ structure corresponds to the 3,4T1 topology recently found in $K_2Cu(SO_4)_2$ (Zhou *et al*., 2020). The natural tiling of the net is formed by $[4^2.10^2]$ and $[6.8.10^2]$ tiles in 1:2 ratio (Fig. 9). Cages corresponding to the tiles form a 3-periodic channel system (Fig. 8*b*). The widest channels run along *c* axis and have spiral like shape.

3.4 Evaluation of percolation threshold energies of ionic motion by BVEL calculations

In order to evaluate possible pathways of mobile ions in the group of natural and synthetic framework copper sulfates, we used BV-based energy calculations as a computationally cheap and time-saving method for a screening of the materials in question. The classic method of crystal structure validation based on bond-valence sums (see, e.g. Brown, 2009, 2016), is thereby supplemented by an approach which benefits from the known positive correlation between ion-conduction pathways and maps of low bond valence mismatch (Adams, 2000; Adams & Prasada Rao, 2011). The construction of bond-valence energy landscapes (BVEL) served to visualize the ion diffusion networks as mappings on energy isosurfaces (Fedotov *et al*., 2018; Katcho *et al*., 2019; Yasui *et al*., 2019). The actual BVEL calculations employed the software 3DBVSMAPPER (Sale & Avdeev, 2012), which generates a spatial distribution of energy values to produce a 3D surface within the unit-cell. For our calculations the spatial resolution was set to 0.2 Å. The bond valence sums for a probe ion (Na^+ or K^+) were calculated and the deviation from the reference value determined. The higher the BV mismatch the higher the energy barriers and thus the lower the ion migration probability.

The threshold value of energy (E_{th}) at which the generated isosurfaces start to percolate the unit cell in at least one dimension can be considered as a rough estimation of the physical activation energy for ion migration. As a caveat it should not be concealed that in some cases E_{th} was reported to differ significantly from the real ion migration energy (Katcho *et al*., 2019). Nevertheless, even though lattice relaxation effects are not taken into account, and despite the relatively low quantitative accuracy of the BVEL method, the results obtained by this approach have been

reported to be in generally good agreement with those obtained by much more demanding quantum mechanical computations (Xiao *et al*., 2015; Deng *et al*., 2018).

We carried out the BVEL screening of all natural and synthetic alkali metal copper sulfates based on 3D frameworks reported so far and listed in Tables 8 and 9. The crystallographic information data and the simplified chemical formulae for mineral phases were used as given in the literature. For the new synthetic $KNaCu(SO_4)_2$ compound the E_{th} energy isosurfaces were calculated separately for each of the alkali metal cations. The results of our calculations of the threshold energies needed for Na^+ and/or K^+ percolation within the unit cell are summarized in Table 9. The table shows that the E_{th} values are relatively high for most of the framework copper sulfates. It is generally accepted that, the values of energy barriers should not exceed 1.6 eV for conducting percolation of alkali metal ions in polyanionic compounds (Adams & Prasada Rao, 2014; Boivin *et al*., 2017). Hence, E_{th} values < 1.6 eV might be an indication of ion transport upon electrochemical cycling. For example, our calculations of E_{th} for alluaudite-type Fe-based sulfate, reported as a promising electrode material (Lu *et al*., 2017) and quoted here as a reference, reveal indeed a value of 1.21 eV for Na^+ migration. Likewise the corresponding calculations for the structure of orthorhombic $KFe(SO_4)F$ show that K^+ ions begin to percolate already at 0.65 eV, in accordance with the reported good reversible potassium insertion/extraction properties (Lander *et al*., 2015).

The tavorite-type $NaCu(SO_4)F$ synthetic phase with the highest theoretical capacity among all the selected copper sulfate framework compounds, displays a very high E_{th} of 4.78 eV, which is in accordance with the experimentally confirmed complete electrochemical inactivity of the compound (Reynaud *et al*., 2012). This is probably due to the specific coordination environment of Na which is strongly bonded by four O^{2-} and one F^- at a short distance of 2.2 Å.

Regardless of its high porosity, the framework of $KNaCu(SO_4)_2$, shows only poor calculated ion diffusion capability for both, Na^+ and K^+ cations as visualized in Fig. 5*e*,*f*. Indeed, the calculated high energy barrier (E_{th} = 2.86 eV) for Na^+ migration is consistent with the results

of electrochemical experiments of the synthetic isotypic $K_2Cu(SO_4)_2$ phase tested at low voltages vs. Na^+/Na, which revealed low capacities and overall structural instability upon cycling (Zhou *et al*., 2020). Again, such limited ability for ion movement is probably due to the stable coordination environments around the alkali cations in the structure of $KNaCu(SO_4)_2$. The bond valence sums of the K1 and Na2 sites localized in the open channels exceed 1 *v.u*. (Table 7) indicating the strong bonding of K^+ and Na^+ ions. The low BVS value for the Na1 site mentioned earlier is probably related with a certain degree of delocalisation along the blue tails shown in Fig. 5*e*,*f*. The valley in the energy landscape where $E_{th} < 1.6$ eV is bounded on both ends by high energy barriers piled up by the surrounding framework.

It is quite interesting that the calculations performed on the isotypic crystal structures of Cs-, Rb-and K-containing cesiodymite and K-only cryptochalcite display relatively low E_{th} values for K^+ percolation. The low E_{th} value of only 1.37 eV found for K^+ percolation in cesiodymite (Fig. 10*a*) is probably due to the substitution of K^+ (ionic radius 1.38 Å) by the big Cs^+ and Rb^+ cations (ionic radii 1.67 Å, and 1.52 Å, respectively) which contributes to the expansion of voids in the framework.

3.5 Modelling of ion migration maps by the analysis of procrystal electron density distribution

As an additional, complementary, method, the search for possible ion migration pathways between particular crystallographic sites and an evaluation of migration barriers was carried out using the IonExplorer program [https://github.com/angolov1990/IonExplorer], which is based on the analysis of procrystal electron density distribution (Downs *et al*., 2002). Within the approach, the diffusion trajectory is approximated by the gradient paths with the lowest electron density values between initial and final positions of mobile ion, while the migration barrier is attributed to the maximum value of electron density along the path. A good agreement of this approach with the results of the NEB(DFT) has been demonstrated recently (Zolotarev *et al*., 2019).

The gradient lines and critical points were calculated by means of the Critic2 program (Otero-de-la-Roza *et al*., 2009). As input information, we used experimental crystallographic data without additional geometry relaxation. The ion diffusion was modeled from a position of the single vacancy hop mechanism. We considered all symmetrically nonequivalent pathways between the neighbor positions in the substructure lattice. The lowest barrier 1-, 2- and 3-dimensional ion migration maps were found, and the electron density profiles were constructed for the pathways within the 3-periodic maps. The term *image* was used (by analogy with NEB-derived energy profiles) to indicate the gradient coordinates in the electron density profiles. For the isotypic crystal structures of saranchinaite and its synthetic analogue, and likewise cryptochalcite and cesiodymite, only models with the sites fully occupied by a single type of alkali metal cations, i.e. ($Na_2Cu(SO_4)_2$ and $K_2Cu_5O(SO_4)_5$), were considered. Structural model with ideal composition $Na_2[CuMg_2(SO_4)_4]$ was used for itelmenite.

Both, BVEL and electron density, approaches give comparable calculated values for potassium (Fig. 11*a*) and sodium (Fig. 11*b*) containing species (*cf*., Tables 9,10,11), and show very good correlation between the results obtained by both methods. The lowest barrier of ionic conductivity among the structures are found for $K_2Cu_5O(SO_4)_5$, $KFeSO_4F$, and $Na_{2.56}[Fe_{1.72}(SO_4)_3]$ (Table 10 and 11). The 1-periodic migration map of $KFeSO_4F$ is piecewise composed of two symmetrically nonequivalent alternating pathways (red and blue in Fig. 12), running along the c axis. In principle, the third migration path (yellow in Fig 12) would link the red/blue one, thereby adding dimensions 2 and 3 to the ion mobility, but this is hampered by the high diffusion barrier along this path (Fig 12*b*). The electron density profiles of the red and blue pathways have convex shape (as seen from below, Fig. 12*b*). This means that cation equilibrium positions at the ends of the pathway are subject to electrostatic repulsion between them. Thus, the introduction of a vacancy at one of the ends of the pathway would lead to shift of cation equilibrium position on the opposite side. Whereas the two Fe-based reference structures were already evaluated for their ion transport properties, finding of a low ion migration barrier for the Cu-containing cryptochalcite

structure is reported here for the first time. Its framework contains two symmetrically non-equivalent channel systems running along the *a* axis which provide the casing for a possible transport of cations (Fig. 10*b*). The 1-periodic ion migration map consists of two symmetrically independent maps, each one being composed of two different alternating partial pieces (red and blue or yellow and green in Fig. 10*c*). Only the red/blue pathway provides a favourably low two barrier migration map (Fig. 10*c*).

The lowest barrier migration map of the reference material $Na_{2.56}[Fe_{1.72}(SO_4)_3]$ is formed by only one type of pathways between Na3 positions (red in Fig. 13). The pathways between Na2 as well as Na1-Na3 and Na1-Na2 positions need much higher activation energy. Thus, only one third of all sodium atoms in the structure are involved in charge transfer, which agrees well with the results of experimental studies, BVSE and DFT calculations reported so far (Wong et al., 2015).

The migration pathways, electron density profiles as well as the lowest barrier periodic migration maps for the full set of the structures are given as supporting materials.

4. Concluding remarks

The present study has demonstrated that compounds consisting of essentially CuO_n polyhedra and SO_4 tetrahedra, with optionally added other species, such as alkali cations Na and K, can indeed form 3*D* framework structures. Such structures could claim interest as materials for potential electrochemical applications, in particular, when they contain alkali cations able to migrate through the framework without impeding its integrity and stability. Mineralogical investigations of active fumaroles have disclosed the existence of plenty of new minerals in the Cu - SO_4 - (+-alkali +- other species) systems; not all of them could have been synthesized so far. This is probably due to the enormous diversity of the physico-chemical conditions under which minerals grow under fumarolic conditions and which cannot easily be screened in the laboratory. These variable conditions concern e.g. chemical composition of fumarolic gases, nature of a

substrate, temperature, pressure, oxygen fugacity, humidity, ... which vary often over short distances and on short time scales, thus creating a myriad of different local "test-tubes".

In view of possible electrochemical applications it must be admitted that, even if suitable minerals were found and the conditions under which they grew were known and could be emulated in the laboratory, much material scientific engineering would probably be necessary before practical applications could be envisaged.

In terms of crystal chemistry the structure determination of the two new synthetic compounds in the system has disclosed that "soft" Cu-O_n polyhedra react rather sensitive to the crystalline environment, which in this case is formed by "hard" SO_4 tetrahedra and Na or K in their usual coordination. Cu has not less than four different coordination polyhedra in the first compound, and in the second compound the single (distorted) Cu octahedron is corner- as well as edge-connected with SO_4 tetrahedra. These observations demonstrate the high structural flexibility of the considered Cu - SO_4 (-alkali metals) systems.

The stoichiometry of the composition of the new compounds described herein was only very recently discovered in minerals, prior to that it was unknown in anhydrous sulfates. Thus, the stoichiometry of the new $K_2Cu_3(SO_4)_4$ phase corresponds to that of itelmenite $Na_2CuMg_2(SO_4)_4$ (Nazarchuk *et al*., 2018), and $KNaCu(SO_4)_2$ is isotypic with saranchinaite $Na_2Cu(SO_4)_2$ (Siidra *et al*., 2018*a*). At the same time, both new compounds exhibit unique structure types, which in turn shows anhydrous sulfates to be a rich family with different polymorphic modifications.

It is worth of notice that the mere observation of structurally dense architectures in minerals and synthetic compounds without alkaline cations in the considered system (Table 8) does not *a priori* exclude the possibility of (de)intercalation properties as shown by the recent discovery and description of yet another fumarolic mineral, koryakite $NaKMg_2Al_2(SO_4)_6$ (Siidra *et al*., 2020*b*) with a framework topology identical to that of millosevichite $Al_2(SO_4)_3$ (Dahmen & Gruehn, 1993) and mikasaite $Fe^{3+}_2(SO_4)_3$ (Christidis & Rentzeperis, 1976). Replacing part of the trivalent cations in the framework by divalent ones provides a negative charge to the framework and allows the

incorporation of alkali species in the channels, which are void in millosevichite and mikasaite. This structural mechanism is known as the concept of stuffed derivative structures first proposed by Buerger (1954).

The BVEL approach demonstrated to be a useful method for the prediction of the mobility of alkali metal ions in various structures. By means of this approach, the threshold energies at which isosurfaces begin to percolate were determined as well as the directions of the ion migration in structures.

The modelling of ion migration maps by the analysis of procrystal electron density distribution was used to perform fast identification of ion migration pathways and limiting barriers between particular crystallographic sites in the structures under consideration. Its consistency and complementarity with the BVEL method have been shown.

Both approaches revealed a relatively low ion threshold percolation and migration barriers in the cryptochalcite-type structures. Thus one may assume the suitability of its 3*D* framework type for ion transport applications. Additional studies are required to investigate experimentally the conductive properties of the cryptochalcite-type compounds, and it is expected to be reported in our next works. We also note that the performed short review did not reveal a correlation between the porosity of the framework structure and the manifestation of ion conduction properties (Figure S1).

Acknowledgements This work was financially supported by the Russian Science Foundation through the grant 16-17-10085. Technical support by the SPbSU X-ray Diffraction Resource Center is gratefully acknowledged. A.S.B. was supported by the internal SPbSU travel grant to the University of Kiel.

References

- Adams, S. & Prasada Rao, R. (2011). High power lithium ion battery materials by computational design. *Phys. Status Solidi*. **208**, 1746–1753.
- Adams, S. & Prasada Rao, R. (2014). Understanding ionic conduction and energy storage materials with bond-valence-based methods. *Bond Valences. Structure and Bonding.* **158**, edited by I.D. Brown & K.R. Poeppelmeier, pp. 129–159. Berlin, Heidelberg: Springer.
- Adams, S. (2000). Modelling ion conduction pathways by bond valence pseudopotential maps. *Solid State Ionics*. **136**–**137**, 1351–1361.
- Balić-Žunić, T., Garavelli, A., Acquafredda, P., Leonardsen, E. & Jakobsson, S. P. (2009). Eldfellite, $NaFe(SO_4)_2$, a new fumarolic mineral from Eldfell volcano, Iceland. *Mineral. Mag.* **73**, 51-57.
- Barpanda, P. (2015). Sulfate chemistry for high-voltage insertion materials: synthetic, structural and electrochemical insights. *Isr. J. Chem.* **55**, 537–557.
- Barpanda, P., Oyama, G., Ling, C. D. & Yamada, A. (2014). Kröhnkite-type $Na_2Fe(SO_4)_2{\cdot}2H_2O$ as a novel 3.25 V insertion compound for Na-ion batteries. *Chem. Mater.* **26**, 1297–1299.
- Ben Yahia, H., Shikano, M. & Yamaguchi, Y. (2016). Li_2CuVO_4: a high capacity positive electrode material for Li-ion batteries. *J. Power Sources.* **320**, 43–48.
- Binnewies, M., Glaum, R., Schmidt, M. & Schmidt, P. (2013). Chemical vapor transport reactions - a historical review. *Z. Anorg. Allg. Chem.* **639**, 219–229.
- Blatov, V. A., Delgado-Friedrichs, O., O'Keeffe, M. & Proserpio, D. M. (2007). Three-periodic nets and tilings: natural tilings for nets. *Acta Cryst.* **A63**, 418-425.
- Blatov, V. A., O'Keeffe, M. & Proserpio, D. M. (2010). Vertex-, face-, point-, Schläfli-, and Delaney-symbols in nets, polyhedra and tilings: recommended terminology. *CrystEngComm*. **12**, 44-48.
- Blatov, V. A., Shevchenko, A. P. & Proserpio, D. M. (2014). Applied topological analysis of crystal structures with the program package ToposPro. *Cryst. Growth Des.* **14**, 3576-3586.
- Boivin, E., Chotard, J.-N., Bamine, T., Carlier, D., Serras, P., Palomares, V., Rojo, T., Iadecola, A., Dupont, L., Bourgeois, L., Fauth, F., Masquelier, C. & Croguennec, L. (2017). Vanadyl-type defects in tavorite-like $NaVPO_4F$: from the average long range structure to local environments. *J. Mater. Chem. A*. **5**, 25044–25055.
- Brown, I. D. & Shannon, R.D. (1973). Empirical bond-strength-bond-length curves for oxides *Acta Cryst. A*29, 266-282.
- Brown, I. D. (2009). Recent developments in the methods and applications of the bond valence model. *Chem. Rev.* **109**, 6858–6919.

- Brown, I. D. (2016). The chemical bond in inorganic chemistry: the bond valence model. Second Edition, *Oxford University Press*, USA.
- Bruker (2014). APEX2. Bruker-AXS Inc., Madison, Wisconsin, USA.
- Buerger, M. J. (1954). The stuffed derivatives of the silica structures. *Amer. Mineral.* **39**, 600-614.
- Burns, P. C. & Hawthorne, F. C. (1995). Coordination-geometry structural pathways in Cu^{2+} oxysalt minerals. *Can. mineral.* **33**, 889-905.
- Christidis, P. C. & Rentzeperis, P. J. (1976). The crystal structure of rhombohedral $Fe_2(SO_4)_3$. *Z. Kristallogr.* **144**, 341-352.
- Dahmen, T. & Gruehn, R. (1993). Beiträge zum thermischen Verhalten von Sulfaten. IX. Einkristallstrukturverfeinerung der Metall(III)-sulfate $Cr_2(SO_4)_3$ und $Al_2(SO_4)_3$. *Z. Kristallogr.* **204**, 57-65.
- Deng, Y., Eames, C., Nguyen, L. H. B., Pecher, O., Griffith, K. J., Courty, M., Fleutot, B., Chotard, J.-N., Grey, C. P., Islam, M. S. & Masquelier, C. (2018). Crystal structures, local atomic environments, and ion diffusion mechanisms of scandium-substituted sodium superionic conductor (NASICON) solid electrolytes. *Chem. Mater.* **30**, 2618–2630.
- Downs, R. T., Gibbs, G. V., Boisen Jr, M. B. & Rosso, K. M. (2002). A comparison of procrystal and ab initio model representations of the electron-density distributions of minerals. *Phys. Chem. Miner.* **29**, 369–385.
- Effenberger, H. (1985). $Cu_2O(SO_4)$, dolerophanite: refinement of the crystal structure, with a comparison of $[OCu(II)_4]$ tetrahedra in inorganic compounds. *Monatsh. Chem.* **116**, 927–931.
- Fedotov, S. S., Kabanova, N. A., Kabanov, A. A., Blatov, V. A., Khasanova, N. R. & Antipov, E. V. (2018). Crystallochemical tools in the search for cathode materials of rechargeable Na-ion batteries and analysis of their transport properties. *Solid State Ionics*. **314**, 129–140.
- Giacovazzo, C., Scandale, E. & Scordari, F. (1976). The crystal structure of chlorotionite, $CuK_2Cl_2SO_4$. *Z. Kristallogr.* **144**, 226-237.
- Goodenough, J. B. & Park, K.-S. (2013). The Li-ion rechargeable battery: a perspective. *J. Am. Chem. Soc.* **135**, 1167-1176.
- Hawthorne, F. C., Burns, P. C. & Krivovichev, S. V. (2000). The crystal chemistry of sulfate minerals. *Rev. Mineral. Geochem.* **40**, 1-112.
- Katcho, N. A., Carrete, J., Reynaud, M., Rousse, G., Casas-Cabanas, M., Mingo, N., Rodríguez-Carvajal, J. & Carrasco, J. (2019). An investigation of the structural properties

of Li and Na fast ion conductors using high-throughput bond-valence calculations and machine learning. *J. Appl. Crystallogr.* **52**, 148–157.

- Kovrugin, V. M., Nekrasova, D. O., Siidra, O. I., Mentré, O., Masquelier, C., Stefanovich, S. Yu. & Colmont, M. (2019). Mineral-inspired crystal growth and physical properties of $Na_2Cu(SO_4)_2$ and review of $Na_2M(SO_4)_2(H_2O)_x$ (x = 0–6) compounds. *Cryst. Growth Des.* **19**, 1233-1244.
- Krivovichev, S. V., Mentré, O., Siidra, O. I., Colmont, M. & Filatov, S. K. (2013). Anion-centered tetrahedra in inorganic compounds. *Chem. Rev.* **113**, 6459-6535.
- Lander, L., Rousse, G., Abakumov, A. M., Sougrati, M., van Tendeloo, G. & Tarascon, J.-M. (2015). Structural, electrochemical and magnetic properties of a novel $KFeSO_4F$ polymorph. *J. Mater. Chem. A*. **3**, 19754–19764.
- Lander, L., Rousse, G., Batuk, D., Colin, C. V., Dalla Corte, D. A. & Tarascon, J.-M. (2017). Synthesis, structure, and electrochemical properties of K-based sulfates $K_2M_2(SO_4)_3$ with M = Fe and Cu. *Inorg. Chem.* **56**, 2013-2021.
- Lander, L., Tarascon, J. M. & Yamada, A. (2018). Sulfate-based cathode materials for Li- and Na-ion batteries. *Chem. Rec.* **18**, 1394-1408.
- Lu, J., Nishimura, S. & Yamada, A. (2017). Polyanionic solid-solution cathodes for rechargeable batteries. *Chem. Mater.* **29**, 3597–3602.
- Masquelier, C. & Croguennec, L. (2013). Polyanionic (phosphates, silicates, sulfates) frameworks as electrode materials for rechargeable Li (or Na) batteries. *Chem. Rev.* **113**, 6552-6591.
- Nazarchuk, E. V., Siidra, O. I., Agakhanov, A. A., Lukina, E. A., Avdontseva, E. Yu. & Karpov, G. A. (2018). Itelmenite, $Na_2CuMg_2(SO_4)_4$, a new anhydrous sulfate mineral from the Tolbachik volcano. *Mineral. Mag.* **82**, 1233-1241.
- Nazarchuk, E. V., Siidra, O. I., Nekrasova, D. O., Shilovskikh, V. V., Borisov A. S. & Avdontseva, E. Yu. (2020). Glikinite, $Zn_3O(SO_4)_2$, a new anhydrous zinc oxysulfate mineral structurally based on OZn_4 tetrahedra. *Mineral. Mag.,* in press. DOI: 10.1180/mgm.2020.33
- Otero-de-la-Roza, A., Blanco, M. A., Martín Pendás, A. & Luaña, V. (2009). Critic: a new program for the topological analysis of solid-state electron densities. *Comput. Phys. Comm.* **180**, 157–166.
- Pekov, I. V., Zubkova, N. V., Agakhanov, A. A., Pushcharovsky, D. Y., Yapaskurt, V. O., Belakovskiy, D. I., Vigasina, M. F., Sidorov, E. G. & Britvin S. N. (2018). Cryptochalcite, $K_2Cu_5O(SO_4)_5$, and cesiodymite, $CsKCu_5O(SO_4)_5$, two new isotypic minerals and the K–Cs isomorphism in this solid-solution series. *Eur. J. Mineral.* **30**, 593–607.

- Pekov, I. V., Zubkova, N. V., Agakhanov, A. A., Yapaskurt, V. O., Chukanov, N. V., Belakovskiy, D. I., Sidorov, E. G. & Pushcharovsky, D. Y. (2017). Dravertite, $CuMg(SO_4)_2$, a new mineral species from the Tolbachik volcano, Kamchatka, Russia. *Eur. J. Mineral.* **29**, 323 – 330.
- Reynaud, M., Barpanda, P., Rousse, G., Chotard, J.-N., Melot, B. C., Recham, N. & Tarascon, J.-M. (2012). Synthesis and crystal chemistry of the Na*M*SO_4F family (*M* = Mg, Fe, Co, Cu, Zn). *Solid State Sci.* **14**, 15–20.
- Reynaud, M., Rousse, G., Abakumov, A. M., Sougrati, M. T., Van Tendeloo, G., Chotard, J.-N. & Tarascon, J.-M. (2014). Design of new electrode materials for Li-ion and Na-ion batteries from the bloedite mineral $Na_2Mg(SO_4)_2{\cdot}4H_2O$. *J. Mater. Chem. A.* **2**, 2671–2680.
- Ri, G.-C., Choe, S.-H. & Yu, C.-J. (2018). First-principles study of mixed eldfellite compounds $Na_x(Fe_{1/2}M_{1/2})(SO_4)_2$ (x=0–2, M = Mn, Co, Ni): a new family of high electrode potential cathodes for the sodium-ion battery. *J. Power Sources.* **378**, 375-382.
- Rousse, G. & Tarascon, J.-M. (2014). Sulfate-based polyanionic compounds for Li-ion batteries: synthesis, crystal chemistry, and electrochemistry aspects. *Chem. Mater.* **26**, 394-406.
- Rozhdestvina, V. I., Udovenko, A. A., Rubanov, S. V. & Mudrovskaya, N. V. (2016). Structural investigation of cooperite (PtS) crystals. *Crystallogr. Rep.* **61**, 193-202.
- Sale, M. & Avdeev, M. (2012). 3DBVSMAPPER: a program for automatically generating bond-valence sum landscapes. *J. Appl. Crystallogr.* **45**, 1054–1056.
- Sheldrick, G. M. (2015). New features added to the refinement program SHELXL since 2008 are described and explained. *Acta Cryst.* **C71**, 3–8.
- Siidra, O. I., Borisov, A. S., Lukina, E. A., Depmeier, W., Platonova, N. V., Colmont, M. & Nekrasova, D. O. (2019*a*). Reversible hydration/dehydration and thermal expansion of euchlorine, ideally $KNaCu_3O(SO_4)_3$. *Phys. Chem. Miner.* **46**, 403–416.
- Siidra, O. I., Lukina, E. A., Nazarchuk, E. V., Depmeier, W., Bubnova, R. S., Agakhanov, A. A., Avdontseva, E. Yu., Filatov, S. K. & Kovrugin, V. M. (2018*a*). Saranchinaite, $Na_2Cu(SO_4)_2$, a new exhalative mineral from Tolbachik volcano, Kamchatka, Russia, and a product of the reversible dehydration of kröhnkite, $Na_2Cu(SO_4)_2(H_2O)_2$. *Mineral. Mag.* **82**, 257-274.
- Siidra, O. I., Nazarchuk, E. V., Agakhanov, A. A. & Polekhovsky, Yu. S. (2019*b*). Aleutite $[Cu_5O_2](AsO_4)(VO_4){\cdot}(Cu_{0.5}\square_{0.5})Cl$, a new complex salt-inclusion mineral with Cu^{2+} substructure derived from Kagome-net. *Mineral. Mag.* **83**, 847-853.
- Siidra, O. I., Nazarchuk, E. V., Agakhanov, A. A., Lukina, E. A., Zaitsev, A. N., Turner, R., Filatov, S. K., Pekov, I. V., Karpov, G. A. & Yapaskurt, V. O. (2018*b*).

Hermannjahnite, $CuZn(SO_4)_2$, a new mineral with chalcocyanite derivative structure from the Naboko scoria cone of the 2012–2013 fissure eruption at Tolbachik volcano, Kamchatka, Russia. *Miner. Petrol.* **112**, 123–134.

- Siidra, O. I., Nazarchuk, E. V., Lukina, E. A., Zaitsev, A. N. & Shilovskikh, V. V. (2018*c*). Belousovite, $KZn(SO_4)Cl$, a new sulphate mineral from the Tolbachik volcano with apophyllite sheet-topology. *Mineral. Mag.* **82**, 1079-1088.
- Siidra, O. I., Nazarchuk, E. V., Zaitsev, A. N. & Shilovskikh, V. V. (2020*a*). Majzlanite, $K_2Na(ZnNa)Ca(SO_4)_4$, a new anhydrous sulphate mineral with complex cation substitutions from Tolbachik volcano. *Mineral. Mag.* **84**, 153-158.
- Siidra, O. I., Nazarchuk, E. V., Zaitsev, A. N. & Vlasenko, N. S. (2020*b*). Koryakite, $NaKMg_2Al_2(SO_4)_6$, a new NASICON-related anhydrous sulphate mineral from Tolbachik volcano. *Mineral. Mag.*, in press. DOI: 10.1180/mgm.2019.69
- Siidra, O. I., Nazarchuk, E. V., Zaitsev, A. N., Lukina, E. A., Avdontseva, E. Yu., Vergasova, L. P., Vlasenko, N. S., Filatov, S. K., Turner, R. & Karpov, G. A. (2017). Copper oxosulphates from fumaroles of Tolbachik volcano: puninite, $Na_2Cu_3O(SO_4)_3$ – a new mineral species and structure refinements of kamchatkite and alumoklyuchevskite. *Eur. J. Mineral.* **29**, 499 – 510.
- Siidra, O. I., Nazarchuk, E. V., Zaitsev, A. N., Polekhovsky, Yu. S., Wenzel, T. & Spratt, J. (2019*c*). Dokuchaevite, $Cu_8O_2(VO_4)_3Cl_3$, a new mineral with remarkably diverse Cu^{2+} mixed-ligand coordination environments. *Mineral. Mag.* **83**, 749-755.
- Singh, P., Shiva, K., Celio, H. & Goodenough, J. B. (2015). Eldfellite, $NaFe(SO_4)_2$: an intercalation cathode host for low-cost Na-ion batteries. *Energy Environ. Sci.* **8**, 3000-3005.
- Starova, G. L., Filatov, S. K., Fundamenskii, V. S. & Vergasova, L. P. (1991). The crystal structure of fedotovite, $K_2Cu_3O(SO_4)_3$. *Mineral. Mag.* **55**, 613-616.
- Sun, M., Rousse, G., Abakumov, A. M., Saubanère, M., Doublet, M.-L., Rodríguez-Carvajal, J., Van Tendeloo, G. & Tarascon, J.-M. (2015). $Li_2Cu_2O(SO_4)_2$: a possible electrode for sustainable Li-based batteries showing a 4.7 V redox activity vs Li^+/Li^0. *Chem. Mater.* **27**, 3077–3087.
- Sun, Y., Guo, S. & Zhou, H. (2019). Exploration of advanced electrode materials for rechargeable sodium-ion batteries. *Adv. Energy Mater.* **9**, 1800212.
- Trussov, I. A., Driscoll, L. L., Male, L. L., Sanjuan, M. L., Orera, A. & Slater, P. R. (2019). Synthesis and structures of sodium containing $K_{2-x}Na_xMg_2(SO_4)_3$ langbeinite phases. *J. Solid State Chem.* **276**, 37-46.

- Waroquiers, D., Gonze, X., Rignanese, G.-M., Welker-Nieuwoudt, C., Rosowski, F., Göbel, M., Schenk, S., Degelmann, P., André, R., Glaum, R. & Hautier, G. (2017). Statistical analysis of coordination environments in oxides. *Chem. Mater.* **29**, 8346-8360.
- Watcharatharapong, T., T-Thienprasert, J., Barpanda, P., Ahuja, R. & Chakraborty, S. (2017). Mechanistic study of Na-ion diffusion and small polaron formation in kröhnkite $Na_2Fe(SO_4)_2 \cdot 2H_2O$ based cathode materials. *J. Mater. Chem. A.* **5**, 21726–21739.
- Wildner, M. & Giester, G. (1988). Crystal structure refinements of synthetic chalcocyanite ($CuSO_4$) and zincosite ($ZnSO_4$). *Miner. Petrol.* **39**, 201-209.
- Wildner, M. (1992). On the geometry of $Co(II)O_6$ polyhedra in inorganic compounds. *Z. Kristallogr.* **202**, 51–70.
- Wong, L. Chen, H. & Adams, S. (2015). Sodium-ion diffusion mechanisms in the low cost high voltage cathode material $Na_{2+\delta}Fe_{2-\delta/2}(SO_4)_3$. *Phys. Chem. Chem. Phys.* **17**, 9186-9193.
- Xiao, R., Li, H. & Chen, L. (2015). High-throughput design and optimization of fast lithium ion conductors by the combination of bond-valence method and density functional theory. *Sci. Rep.* **5**, 14227.
- Xu, S.-Y., Wu, X.-Y., Li, Y.-M., Hu, Y.-S. & Chen, L.-Q. (2014). Novel copper redox-based cathode materials for room-temperature sodium-ion batteries. *Chinese Phys. B.* **23**, 118202.
- Yasui, Y., Niwa, E., Matsui, M., Fujii, K. & Yashima, M. (2019). Discovery of a rare-earth-free oxide-ion conductor $Ca_3Ga_4O_9$ by screening through bond valence-based energy calculations, synthesis, and characterization of structural and transport properties. *Inorg. Chem.* **58**, 9460–9468.
- Yu, C.-J., Choe, S.-H., Ri, G.-C., Kim, S.-C., Ryo, H.-S. & Kim, Y.-J. (2017). Ionic diffusion and electronic transport in eldfellite $Na_xFe(SO_4)_2$. *Phys. Rev. Appl.* **8**, 024029.
- Zhou, H. A., Liu, Z., Ang, S. S. & Zhang, J.-J. (2020). Synthesis, structure, and electrochemical performances of a novel three-dimensional framework $K_2[Cu(SO_4)_2]$. *Solid State Sci.* **100**, 106104.
- Zolotarev, P. N., Golov, A. A., Nekrasova, N. A. & Eremin, R. A. (2019). Topological analysis of procrystal electron densities as a tool for computational modeling of solid electrolytes: A case study of known and promising potassium conductors. *AIP Conf. Proc.* **2163**, 020007.

Table 1. Crystallographic data and refinement parameters for $K_2Cu_3(SO_4)_4$ and $KNaCu(SO_4)_2$

	$K_2Cu_3(SO_4)_4$	$KNaCu(SO_4)_2$
Crystal data:		
Temperature	296 K	296 K
Radiation	MoK_α, 0.71073 Å	MoK_α, 0.71073 Å
Crystal system	monoclinic	monoclinic
Space group	*C*2/*c*	*C*2/*c*
a (Å)	13.6088(5)	15.9721(10)
b (Å)	11.9627(5)	9.4576(6)
c (Å)	17.0791(7)	9.0679(6)
β (°)	112.4500(10)	93.6350(10)
Volume (Å^3) / *Z*	2569.72(18) / 8	1367.02(15) / 8
D_{calc} (g/cm^3)	3.376	3.088
μ (mm^{-1})	6.316	4.489
Crystal size (mm^3)	0.10×0.12×0.12	0.16×0.16×0.08
Data collection:		
θ range (°)	2.581– 27.999	2.504 – 27.992
h, *k*, *l* ranges	−17 → 17, −15 → 15, −22 → 21	−21 → 21, −12 → 12, −6 → 11
Total reflections collected	12218	6732
Unique reflections (R_{int})	3093 (0.0282)	1655 (0.0282)
Unique reflections F > 4σF	2746	1452
Structure refinement:		
Weighting scheme *a*, *b*	0.030700, 6.820500	0.037200, 5.92500
Extinction coefficient	0.00040(4)	-
$R_1[F > 4\sigma_F]$, $wR_2[F > 4\sigma_F]$	0.023, 0.059	0.029, 0.035
R_1 all, wR_2 all	0.028, 0.061	0.082, 0.085
Goodness-of-fit	1.027	1.190
Largest diff. peak and hole, e Å^{-3}	1.401, -1.326	0.691, -0.810

Table 2. Coordinates and atomic displacement parameters (Å^2) of atoms in $K_2Cu_3(SO_4)_4$

Atom	*Wyck. letter*	*x*	*y*	*z*	U_{eq}	U_{11}	U_{22}	U_{33}	U_{23}	U_{13}	U_{12}
Cu1	8*f*	0.18027(3)	0.37478(2)	0.37549(2)	0.01083(9)	0.01413(16)	0.00772(15)	0.01048(17)	0.00070(11)	0.00450(13)	-0.00134(11)
Cu2	4*a*	0	0	½	0.01035(11)	0.0139(2)	0.0104(2)	0.0073(2)	-0.00205(16)	0.00475(17)	-0.00380(16)
Cu3	8*f*	0.21091(3)	-0.11938(2)	0.38223(2)	0.01233(9)	0.02120(17)	0.00811(15)	0.00734(17)	0.00014(11)	0.00507(13)	0.00284(12)
Cu4	4*e*	½	0.17223(4)	¼	0.02095(13)	0.0423(3)	0.0084(2)	0.0185(3)	0	0.0187(2)	0
S1	8*f*	0.15707(5)	0.12584(5)	0.43030(4)	0.00891(13)	0.0122(3)	0.0062(3)	0.0090(3)	0.0004(2)	0.0048(2)	0.0000(2)
S2	8*f*	0.25976(5)	0.62829(5)	0.42973(4)	0.00921(13)	0.0128(3)	0.0072(3)	0.0081(3)	-0.0001(2)	0.0045(2)	0.0006(2)
S3	8*f*	0.39868(5)	0.35893(5)	0.32593 (4)	0.01143(13)	0.0180(3)	0.0088(3)	0.0068(3)	-0.0008(2)	0.0040(2)	-0.0030(2)
S4	8*f*	0.07333(5)	0.45584(5)	0.17289(4)	0.01247(14)	0.0155(3)	0.0104(3)	0.0129(3)	-0.0006(2)	0.0070(3)	0.0012(2)
K1	8*f*	0.48159(6)	0.16244(5)	0.47511(4)	0.02471(15)	0.0364(4)	0.0189(3)	0.0179(3)	0.0045(2)	0.0093(3)	0.0024(3)
K2	8*f*	0.32922(9)	0.63841(6)	0.26592(6)	0.04422(2)	0.0934(7)	0.0227(3)	0.0372(5)	0.0092(3)	0.0480(5)	0.0136(4)
O1	8*f*	0.44236(14)	0.45639(15)	0.38073(11)	0.0130(4)	0.0190(9)	0.0122(8)	0.0071(9)	-0.0031(7)	0.0043(7)	-0.0034(7)
O2	8*f*	0.13143(15)	0.21999(15)	0.36936(12)	0.0145(4)	0.0198(9)	0.0100(8)	0.0130(10)	0.0029(7)	0.0055(8)	-0.0017(7)
O3	8*f*	0.32584(16)	0.29510(16)	0.35344(13)	0.0205(4)	0.0242(10)	0.0179(10)	0.0177(11)	0.0025(8)	0.0060(9)	-0.0091(8)
O4	8*f*	0.23614(15)	0.52527(15)	0.37897(12)	0.0139(4)	0.0218(9)	0.0090(8)	0.0127(10)	-0.0020(7)	0.0084(8)	-0.0015(7)
O5	8*f*	0.07879(16)	0.12492(14)	0.47042(13)	0.0153(4)	0.0218(10)	0.0131(9)	0.0157(10)	-0.0028(7)	0.0124(8)	-0.0039(7)
O6	8*f*	0.21119(16)	0.62686(15)	0.49384(13)	0.0148(4)	0.0195(9)	0.0166(9)	0.0092(10)	0.0004(7)	0.0066(8)	0.0012(7)
O7	8*f*	0.20966(16)	0.71908(15)	0.36657(12)	0.0163(4)	0.0291(11)	0.0092(8)	0.0098(10)	0.0018(7)	0.0066(8)	0.0039(8)
O8	8*f*	0.14523(15)	0.02496(15)	0.37808(13)	0.0162(4)	0.0203(9)	0.0112(8)	0.0164(11)	-0.0041(7)	0.0062(8)	0.0016(7)
O9	8*f*	0.48903(17)	0.28597(16)	0.32932(13)	0.0199(4)	0.0312(11)	0.0126(9)	0.0167(11)	-0.0022(8)	0.0100(9)	0.0045(8)
O10	8*f*	0.11225(17)	0.37378(16)	0.24151(14)	0.0209(5)	0.0253(11)	0.0146(9)	0.0233(12)	0.0049(8)	0.0100(9)	0.0021(8)
O11	8*f*	0.26564(15)	0.13447(15)	0.49377(13)	0.0165(4)	0.0138(9)	0.0159(9)	0.0168(11)	0.0005(8)	0.0024(8)	-0.0007(7)
O12	8*f*	0.34385(18)	0.40389(16)	0.24056(13)	0.0206(4)	0.0357(12)	0.0153(9)	0.0072(10)	0.0002(8)	0.0042(9)	0.0000(9)
O13	8*f*	0.13710(17)	0.45542(19)	0.12049(14)	0.0256(5)	0.0249(11)	0.0346(12)	0.0230(12)	0.0045(10)	0.0154(10)	0.0078(9)
O14	8*f*	0.37427(15)	0.64563(16)	0.46935(14)	0.0193(4)	0.0125(9)	0.0178(9)	0.0253(12)	-0.0041(8)	0.0047(8)	-0.0005(7)
O15	8*f*	-0.03675(16)	0.43245(19)	0.11633(14)	0.0260(5)	0.0188(10)	0.0371(13)	0.0203(12)	-0.0031(10)	0.0052(9)	-0.0044(9)
O16	8*f*	0.07908(19)	0.57047(16)	0.20782(14)	0.0252(5)	0.0409(13)	0.0120(9)	0.0224(12)	-0.0036(8)	0.0118(10)	0.0030(9)

Table 3. Coordinates and atomic displacement parameters ($Å^2$) of atoms in $KNaCu(SO_4)_2$

Atom	*Wyck letter*	*x*	*y*	*z*	U_{eq}	U_{11}	U_{22}	U_{33}	U_{23}	U_{13}	U_{12}
Cu1	8*f*	0.13626(3)	0.69568(5)	0.16921(5)	0.01462(14)	0.0130(2)	0.0163(2)	0.0148(2)	0.00030(16)	0.00308(16)	-0.00076(16)
S1	8*f*	0.28562(5)	0.90211(9)	0.14187(9)	0.01156(18)	0.0097(4)	0.0128(4)	0.0123(4)	-0.0014(3)	0.0017(3)	-0.0008(3)
S2	8*f*	-0.02639(5)	0.75891(9)	0.05052(9)	0.01176(18)	0.0121(4)	0.0146(4)	0.0087(4)	0.0004(3)	0.0022(3)	0.0008(3)
K1	8*f*	0.11238(5)	0.93846(8)	-0.18306(9)	0.02035(19)	0.0242(4)	0.0180(4)	0.0185(4)	-0.0014(3)	-0.0012(3)	0.0004(3)
Na1	4*c*	¼	¾	½	0.0164(4)	0.0181(10)	0.0177(10)	0.0123(9)	-0.0033(8)	-0.0073(7)	0.0049(8)
Na2	4*e*	0	0.5682(2)	-¼	0.0236(5)	0.0305(12)	0.0114(10)	0.0301(12)	0	0.0110(10)	0
O1	8*f*	0.02206(15)	0.6307(3)	0.1012(3)	0.0157(5)	0.0145(12)	0.0171(12)	0.0158(12)	0.0023(10)	0.0035(9)	0.0046(10)
O2	8*f*	0.22461(17)	0.9931(3)	0.0629(3)	0.0262(6)	0.0225(14)	0.0250(14)	0.0298(15)	-0.0002(12)	-0.0079(12)	0.0102(12)
O3	8*f*	0.33740(17)	0.8228(3)	0.0412(3)	0.0239(6)	0.0220(14)	0.0331(16)	0.0181(13)	0.0031(11)	0.0122(11)	0.0100(12)
O4	8*f*	0.24175(17)	0.7929(3)	0.2289(3)	0.0244(6)	0.0175(13)	0.0359(16)	0.0202(14)	0.0068(12)	0.0032(11)	-0.0129(12)
O5	8*f*	-0.10725(15)	0.7605(3)	0.1253(3)	0.0182(5)	0.0109(12)	0.0253(14)	0.0191(13)	0.0035(11)	0.0053(10)	0.0059(10)
O6	8*f*	-0.04543(17)	0.7551(3)	-0.1080(3)	0.0207(6)	0.0269(14)	0.0252(14)	0.0099(12)	-0.0009(10)	-0.0004(10)	0.0060(11)
O7	8*f*	0.34103(18)	0.9811(3)	0.2465(3)	0.0268(6)	0.0313(16)	0.0173(13)	0.0296(15)	-0.0057(11)	-0.0154(12)	-0.0028(12)
O8	8*f*	0.02487(18)	0.8821(3)	0.0935(3)	0.0231(6)	0.0287(15)	0.0212(14)	0.0195(13)	-0.0003(11)	0.0036(11)	-0.0115(11)

Table 4. Selected interatomic distances (Å) and angles (degrees) in $K_2Cu_3(SO_4)_4$

Cu1-O4$_{eq}$		1.946(2)	S2-O14	1.457(2)	O11-S1-O5	111.18(12)
Cu1-O2$_{eq}$		1.957(2)	S2-O4	1.470(2)	O11-S1-O8	110.62(11)
Cu1-O11$_{eq}$		2.070(2)	S2-O6	1.479(2)	O5-S1-O8	110.18(11)
Cu1-O10$_{eq}$		2.116(2)	S2-O7	1.499(2)	O11-S1-O2	111.51(11)
<Cu1-O$_{eq}$>		2.002	<S2-O>	1.476	O5-S1-O2	108.35(11)
Cu1-O15$_{ap}$		2.126(2)			O8-S1-O2	104.80(12)
Cu1-O3$_{ap}$		2.355(2)			<O-S1-O>	109.44
<Cu1-O$_{ap}$>		2.241				
<Cu1-O$_{tot}$>		2.095				
Cu2-O1$_{eq}$	×2	1.954(2)	S3-O3	1.463(2)	O14-S2-O4	110.33(11)
Cu2-O5$_{eq}$	×2	2.013(2)	S3-O12	1.463(2)	O14-S2-O6	111.03(12)
<Cu2-O$_{eq}$>		1.984	S3-O1	1.471(2)	O4-S2-O6	111.59(11)
Cu2-O14$_{ap}$	×2	2.356(2)	S3-O9	1.491(2)	O14-S2-O7	110.06(12)
<Cu2-O$_{tot}$>		2.108	<S3-O>	1.472	O4-S2-O7	104.24(11)
					O6-S2-O7	109.39(11)
					<O-S2-O>	109.44
Cu3-O8$_{eq}$		1.933(2)	S4-O10	1.464(2)	O12-S3-O3	111.19(12)
Cu3-O7$_{eq}$		1.950(2)	S4-O13	1.465(2)	O12-S3-O1	105.73(11)
Cu3-O12$_{eq}$		1.959(2)	S4-O15	1.466(2)	O3-S3-O1	111.59(12)
Cu3-O6$_{eq}$		1.974(2)	S4-O16	1.486(2)	O12-S3-O9	110.67(12)
<Cu3-O$_{eq}$>		1.954	<S4-O>	1.470	O3-S3-O9	109.38(12)
Cu3-O13$_{ap}$		2.270(2)			O1-S3-O9	108.21(12)
<Cu3-O$_{tot}$>		2.017			<O-S3-O>	109.46
Cu4-O16$_{eq}$	×2	1.937(2)	K1-O15	2.762(2)	O10-S4-O15	111.45(13)
Cu4-O9$_{eq}$	×2	1.966(2)	K1-O3	2.822(2)	O10-S4-O13	111.65(13)
<Cu4-O$_{eq}$>		1.952	K1-O9	2.930(2)	O15-S4-O13	106.94(13)
Cu4-O7$_{ap}$	×2	2.843(2)	K1-O5	2.932(2)	O10-S4-O16	110.49(13)
<Cu4-O$_{tot}$>		2.249	K1-O14	2.932(2)	O15-S4-O16	108.94(13)
			K1-O13	2.936(2)	O13-S4-O16	107.20(13)
			K1-O6	3.047(2)	<O-S4-O>	109.45
			K1-O13	3.065(2)		
			K1-O11	3.093(2)		
			K1-O16	3.112(2)		
			K1-O15	3.386(2)		
			<K1-O>	3.002		
S1-O11		1.465(2)	K2-O2	2.743(2)		
S1-O5		1.470(2)	K2-O12	2.857(2)		
S1-O8		1.472(2)	K2-O1	2.941(2)		
S1-O2		1.482(2)	K2-O10	2.942(2)		
<S1-O>		1.472	K2-O8	2.944(2)		
			K2-O7	2.945(2)		
			K2-O3	2.973(2)		
			K2-O4	3.005(2)		
			K2-O16	3.264(3)		
			K2-O14	3.291(2)		
			<K2-O>	2.991		

Table 5. Selected interatomic distances (Å) and angles (degrees) in $KNaCu(SO_4)_2$

$Cu1\text{-}O4_{eq}$	1.965(3)	K1-O6		2.735(3)	O2-S1-O7	112.14(17)
$Cu1\text{-}O1_{eq}$	1.986(3)	K1-O2		2.819(3)	O2-S1-O3	112.37(17)
$Cu1\text{-}O3_{eq}$	1.987(3)	K1-O3		2.876(3)	O7-S1-O3	108.76(18)
$Cu1\text{-}O5_{eq}$	2.042(3)	K1-O5		2.897(3)	O2-S1-O4	110.23(17)
$<Cu1\text{-}O_{eq}>$	1.995	K1-O8		2.927(3)	O7-S1-O4	107.10(17)
$Cu1\text{-}O7_{ap}$	2.191(3)	K1-O8		2.929(3)	O3-S1-O4	105.94(17)
$Cu1\text{-}O8_{ap}$	2.567(3)	K1-O8		2.995(3)	<O-S1-O>	109.42
$<Cu1\text{-}O_{ap}>$	2.379	K1-O2		3.076(3)		
$<Cu1\text{-}O_{tot}>$	2.123	K1-O6		3.169(3)		
		K1-O4		3.242(3)		
		K1-O4		3.401(3)		
		<K1-O>		3.006		
S1-O2	1.454(3)	Na1-O5	×2	2.484(3)	O6-S2-O8	111.23(16)
S1-O7	1.461(3)	Na1-O4	×2	2.486(3)	O6-S2-O1	110.90(15)
S1-O3	1.475(3)	Na1-O2	×2	2.534(3)	O8-S2-O1	107.12(16)
S1-O4	1.500(3)	<Na1-O>		2.501	O6-S2-O5	108.46(16)
<S1-O>	1.473				O8-S2-O5	110.82(16)
					O1-S2-O5	108.27(14)
					<O-S2-O>	109.47
S2-O6	1.451(3)	Na2-O6	×2	2.330(3)		
S2-O8	1.463(3)	Na2-O1	×2	2.354(3)		
S2-O1	1.495(3)	Na2-O7	×2	2.580(3)		
S2-O5	1.497(2)	<Na2-O>		2.421		
<S2-O>	1.477					

Table 6. Bond-valence analysis (in valence units = *v.u.*) for the crystal structure of $K_2Cu_3(SO_4)_4$

	O1	**O2**	**O3**	**O4**	**O5**	**O6**	**O7**	**O8**	**O9**	**O10**	**O11**	**O12**	**O13**	**O14**	**O15**	**O16**	$\sum_v$c
Cu1		0.47	0.15	0.48						0.30	0.34				0.29		**2.03**
Cu2	0.47×2→				0.40×2→									0.15×2→			**2.04**
Cu3						0.45	0.48	0.50				0.46	0.19				**2.08**
Cu4							0.04×2→		0.46×2→							0.49×2→	**1.98**
K1			0.14		0.11	0.08			0.11		0.07		0.11 0.08	0.11	0.17 0.03	0.07	**1.08**
K2	0.11	0.17	0.10	0.09			0.10	0.11		0.11		0.13		0.04		0.05	**1.01**
S1		1.46			1.51			1.50			1.53						**6.00**
S2				1.51		1.47	1.40							1.56			**5.94**
S3	1.50		1.54						1.43			1.54					**6.01**
S4										1.53			1.53		1.52	1.45	**6.03**
$\sum_v$a	**2.08**	**2.1**	**1.93**	**2.08**	**2.02**	**2.00**	**2.02**	**2.11**	**2.00**	**1.94**	**1.94**	**2.13**	**1.91**	**1.86**	**2.01**	**2.06**	

Table 7. Bond-valence analysis (in valence units = *v.u.*) for the crystal structure of $KNaCu(SO_4)_2$

	O1	**O2**	**O3**	**O4**	**O5**	**O6**	**O7**	**O8**	$\sum_v$c
Cu1	0.43		0.43	0.46	0.37		0.24	0.08	**2.01**
K1		0.14 0.08	0.12	0.05 0.03	0.12	0.18 0.06		0.11×2→↓ 0.09	**1.09**
Na1		0.14×2→		0.15×2→	0.15×2→				**0.88**
Na2	0.21×2→					0.22×2→	0.12×2→		**1.10**
S1		1.57	1.49	1.40			1.54		**6.00**
S2	1.42				1.41	1.58		1.54	**5.94**
$\sum_v$a	**2.06**	**1.93**	**2.04**	**2.09**	**2.05**	**2.04**	**1.90**	**1.93**	

Table 8. List of framework porosity (FP), and framework density (FD) for anhydrous framework copper sulfates.

Formula	**Mineral name**	**Sp. group**	***a*** **(Å)** ***α*** **(deg)**	***b*** **(Å)** ***β*** **(deg)**	***c*** **(Å)** ***γ*** **(deg)**	***V*** **(Å^3)** ***Z***	**FP (%)**	**FD**	**Reference**
$CuZn(SO_4)_2$	Hermannjahnite	$P2_1/n$	4.8076	8.4785 93.041	6.7648	275.35 2	71	29.05	Siidra et al., 2018*b*
$Cu(SO_4)$	Chalcocyanite	*Pnma*	8.4123	6.7040	4.8303	272.41 2	76	29.37	Wildner & Giester, 1988; Siidra et al., 2018*b*
$(Zn,Cu)_3O(SO_4)_2$	Glikinite	$P2_1/m$	7.298	6.588 117.15	7.840	335.4 2	74	29.82	Nazarchuk *et al*., 2020
$Cu_2O(SO_4)$	Dolerophanite	$C2/m$	9.370	6.319 122.34	7.639	382.1 4	73	31.40	Effenberger, 1985

Table 9. List of anhydrous framework (highlighted in formulas in square brackets) copper sulfates with alkali metal cations and values of calculated threshold energies (E_{th}), theoretical capacity for 1 e^- transfer per Cu (C_{th}), framework porosity (FP), and framework density (FD).

Formula		**Sp. group**	***a*** **(Å)** ***α*** **(deg)**	***b*** **(Å)** ***β*** **(deg)**	***c*** **(Å)** ***γ*** **(deg)**	***V*** **(Å^3)** ***Z***	**E_{th} (Na^+, eV)**	**E_{th} (K^+, eV)**	**C_{th} (mAh/g)**	**FP (%)**	**FD**	**Reference**
Natural phases	**Mineral name**											
$Na_{1.92}K_{0.08}[Cu(SO_4)_2]$	Saranchinaite	*P*2$_1$	9.0109	15.6355 107.079	10.1507	1367.062	2.26		88.8	86	17.56	Siidra *et al*., 2018*a*
$Na_{1.98}K_{0.02}[Cu_{1.3}Mg_{1.6}Zn_{0.1}(SO_4)_4]$	Itelmenite	*Pbca*	9.568	8.790	28.715	2415.04	3.30		49.4	79	23.19	Nazarchuk *et al*., 2018
$K[Cu_3O(SO_4)_2]Cl$	Kamchatkite	*Pnma*	9.755	7.0152	12.886	881.88		4.56	40.3	79	22.68	Siidra *et al*., 2017
$K_2[Cu_5O(SO_4)_5]$	Cryptochalcite	*P*-1	10.0045 102.194	12.6663 101.372	14.4397 90.008	1751.74		2.14	30.0	80	22.83	Pekov *et al*., 2018
$K_{1.1}Rb_{0.2}Cs_{0.7}[Cu_5O(SO_4)_5]$	Cesiodymite	*P*-1	10.0682 102.038	12.7860 100.847	14.5486 89.956	1797.54		1.37	27.2	81	22.25	Pekov *et al*., 2018
Synthetic phases	**Str. type**											
$Na[Cu(SO_4)]F$	Tavorite	*C*2/*c*	6.8231	8.5246 110.745	6.8778	374.114	4.78		132.9	81	21.38	Reynaud *et al*., 2012
$Na_2[Cu(SO_4)_2]$	Saranchinaite	*P*2$_1$	8.9711	15.5482 107.155	10.1421	1351.732	2.28		88.8	86	17.76	Kovrugin *et al*., 2019
$KNa[Cu(SO_4)_2]$		*C*2/*c*	15.9721	9.4576 93.6350	9.0679	1367.028	2.86	18.91	84.3	86	17.56	This work
$K_2[Cu(SO_4)_2]$		*C*2/*c*	16.0433	9.7819 93.2680	9.2341	1446.798		15.31	80.3	86	16.59	Zhou *et al*., 2020
$K_2[Cu_3(SO_4)_4]$		*C*2/*c*	13.6088	11.9627 112.4500	17.0791	2569.728		6.62	41.0	82	21.79	This work
Reference phases	**Str. type**											
$K[Fe(SO_4)]F$	$KTiOPO_4$	*Pna*2$_1$	13.15116	6.539302	10.86887	934.7164		0.65	127.6	84	17.12	Lander *et al*., 2015
$Na_{2.56}[Fe_{1.72}(SO_4)_3]$	Alluaudite	*C*2/*c*	12.6556	12.7726 115.5439	6.5144	950.094	1.21		60.5	81	21.05	Lu *et al*., 2017

Table 10. List of anhydrous framework copper and iron sulfates with potassium metal cations and the maximal values of electron density (ρ), along the gradient paths that form 1-, 2-, and 3-periodic map.

Compound	Periodicity	Path	$\rho(a.u.)\times10^4$
$K_2[Cu_5O(SO_4)_5]$	1	0, 1	4.054
	2	0, 1, 2, 3, 5, 4	20.843
	3	0, 1, 2, 3, 5, 4, 9, 8, 18, 21, 20, 17, 27, 10, 29, 11, 26, 33, 24, 32, 12	47.670
$K[FeSO_4F]$	1	0, 1	4.155
	2	-	-
	3	0, 1, 2	7.397
$K[Cu_3O(SO_4)_2]Cl$	1	0	6.753
	2	-	-
	3	0, 2, 1	37.352
$K_2[Cu_3(SO_4)_4]$	1	3, 0, 2	7.400
	2	-	-
	3	3, 0, 2, 1	10.769
$K_2[Cu(SO_4)_2]$	1	0, 1, 2	12.558
	2	-	-
	3	0, 1, 2, 3	12.798

Table 11. List of anhydrous framework copper and iron sulfates with sodium metal cations and the maximal values of electron density (ρ), along the gradient paths that form 1-, 2-, and 3-periodic map.

Compound	Periodicity	Path	$\rho(a.u.)\times10^4$
$Na_{2.56}[Fe_{1.72}(SO_4)_3]$	1	1	9.872
	2	1, 0, 3, 2	20.301
	3	1, 0, 3, 2, 4, 5, 9, 7	65.832
$Na_2[Cu(SO_4)_2]$	1	14, 4, 17, 22, 15, 10, 6, 2	12.312
	2	14, 4, 17, 22, 15, 10, 6, 2, 13, 39, 21, 18, 9, 11, 16, 20, 57, 0	15.907
	3	14, 4, 17, 22, 15, 10, 6, 2, 13, 39, 21, 18, 9, 11, 16, 20, 57, 0, 7	15.951
$Na_2[CuMg_2(SO_4)_4]$	1	-	-
	2	1, 0, 5	17.599
	3	1, 0, 5, 3	17.7445
$Na[CuSO_4F]$	1	1	31.051
	2	-	-
	3	1, 0	33.386

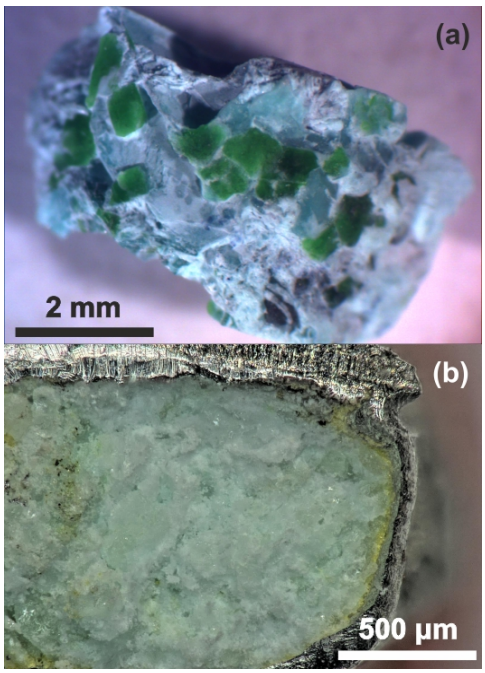

Figure 1. Light-blue crystals of $K_2Cu_3(SO_4)_4$ with green crystals of the synthetic analogue of fedotovite $K_2Cu_3O(SO_4)_3$ ***(a)***. Transparent light-blue crystals of $KNaCu(SO_4)_2$ in the mass of unreacted Na_2SO_4 and small yellow crystals of $K_2(PtCl_6)$ in the rim ***(b)***.

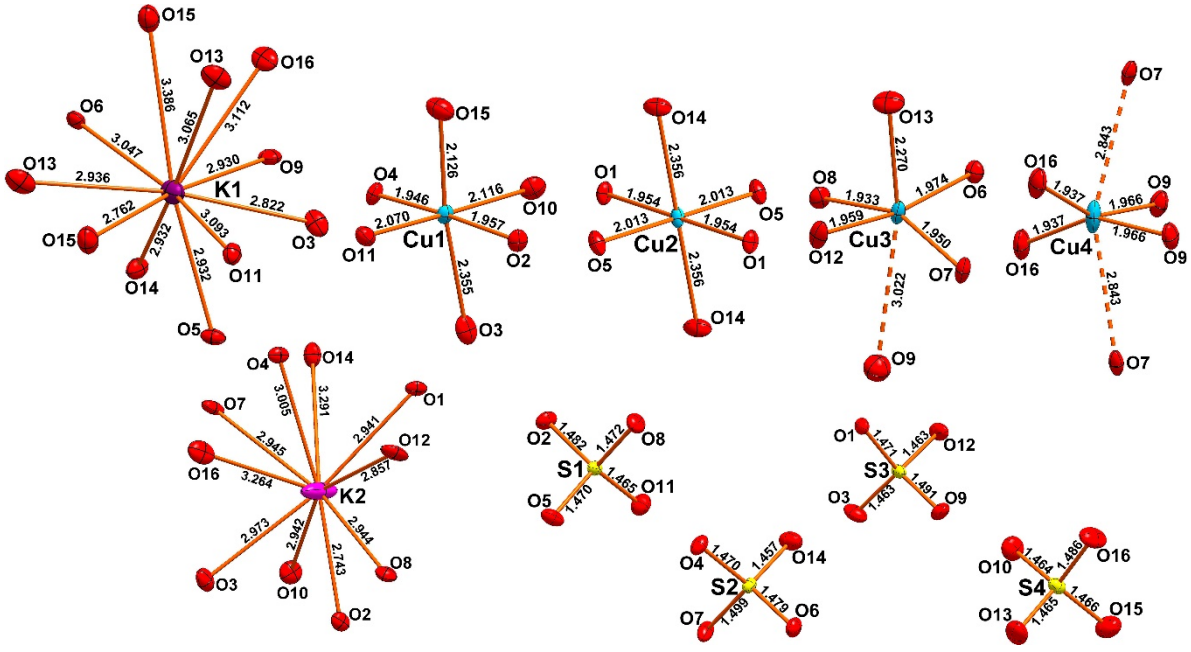

Figure 2. Coordination of cations in the crystal structure of $K_2Cu_3(SO_4)_4$. Legend: K^+ = pink; Cu^{2+} = cyan; S^{6+} = yellow; O^{2-} = red. A.d.p. ellipsoids are drawn at the 50 % probability level. All interatomic distances are given in Å.

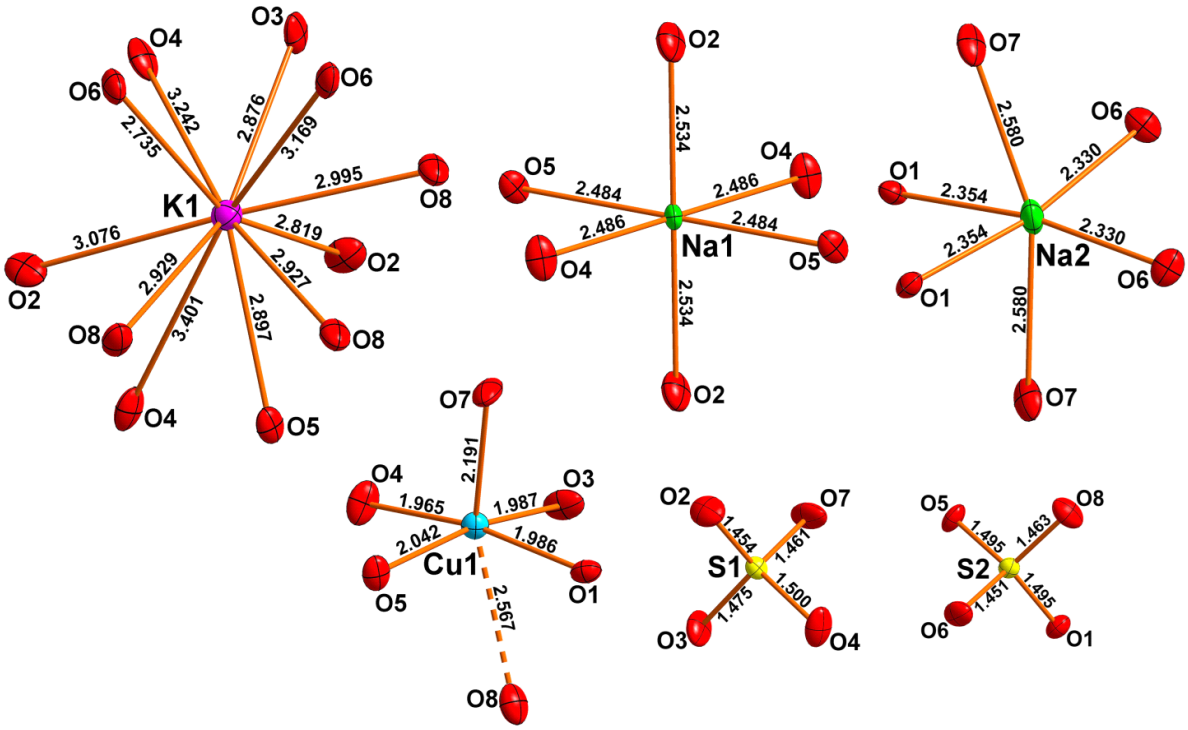

Figure 3. Coordination of cations in the crystal structure of $KNaCu(SO_4)_2$. Legend: K^+ = *pink*; Na^+ = *green*; Cu^{2+} = *cyan*; S^{6+} = *yellow*; O^{2-} = *red*. All interatomic distances are given in Å. A.d.p. ellipsoids are drawn at the 50 % probability level.

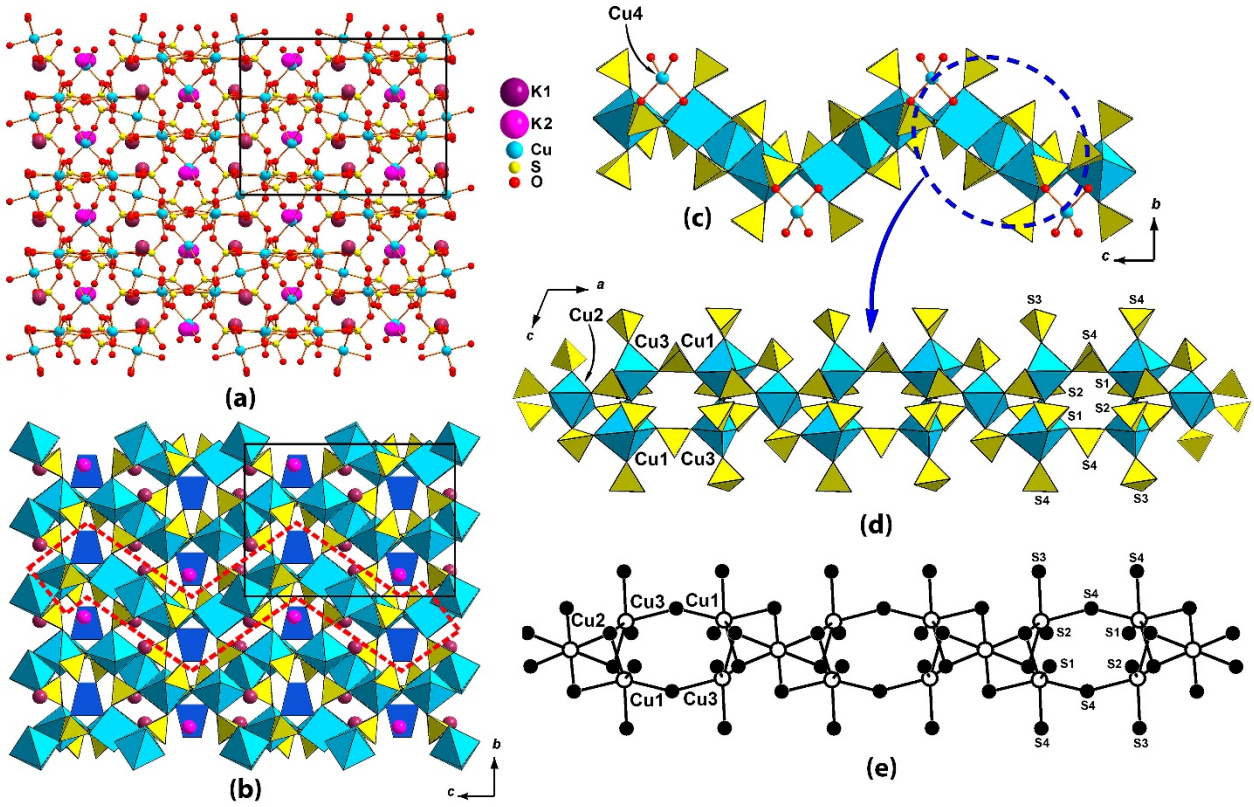

Figure 4. Balls-and-sticks (***a***) and polyhedral (***b***) representation of the crystal structure of $K_2Cu_3(SO_4)_4$ along the *a* axis. Legend: $Cu1O_6$, $Cu2O_6$, $Cu3O_5$ polyhedra = blue; $Cu4O_4$ squares = dark blue; SO_4 tetrahedra = yellow. The $[Cu_3(SO_4)_4]^{2-}$ framework can be split into zig-zag layers highlighted by the red dashed line (***b***,***c***). The layers consist of porous bands (polyhedral representation (***d***) and graph (***e***)).

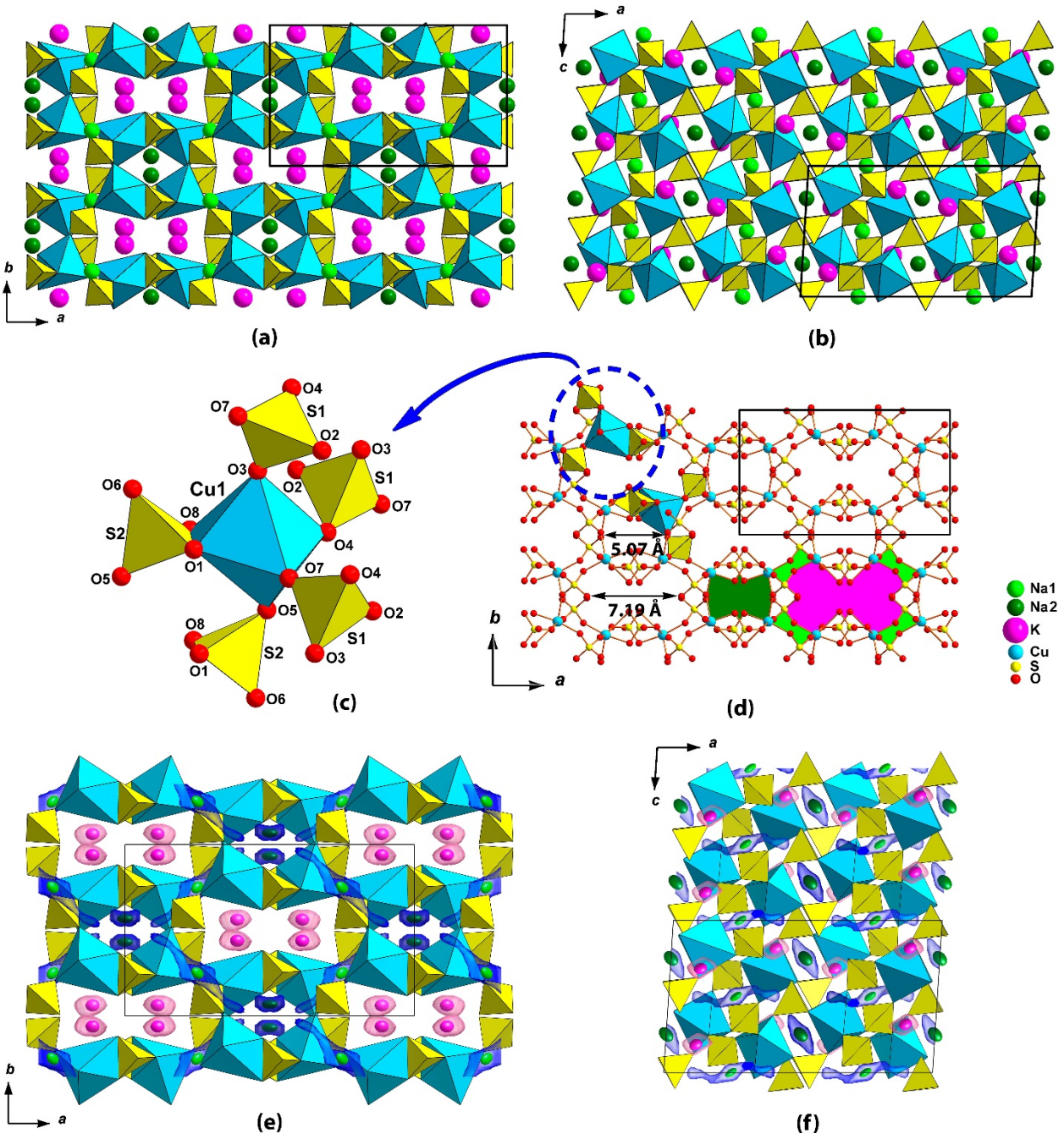

Figure 5. General projections of the crystal structure of $KNaCu(SO_4)_2$ along the *c* (***a***) and *b* (***b***) axes. The $[Cu(SO_4)_2]^{2-}$ framework is formed by corner- and edge-sharing of CuO_6 octahedra with SO_4 tetrahedra (***c***). Larger channels (pink) are occupied by K atoms, whereas the smaller (green) ones by Na atoms in the $[Cu(SO_4)_2]^{2-}$ framework (***d***). The non-interconnected BVEL (blue color for Na^+ and pink for K^+) is plotted at 1.6 eV along the *c* (***e***) and *b* (***f***) axes. A.d.p. ellipsoids are drawn at the 90 % probability level.

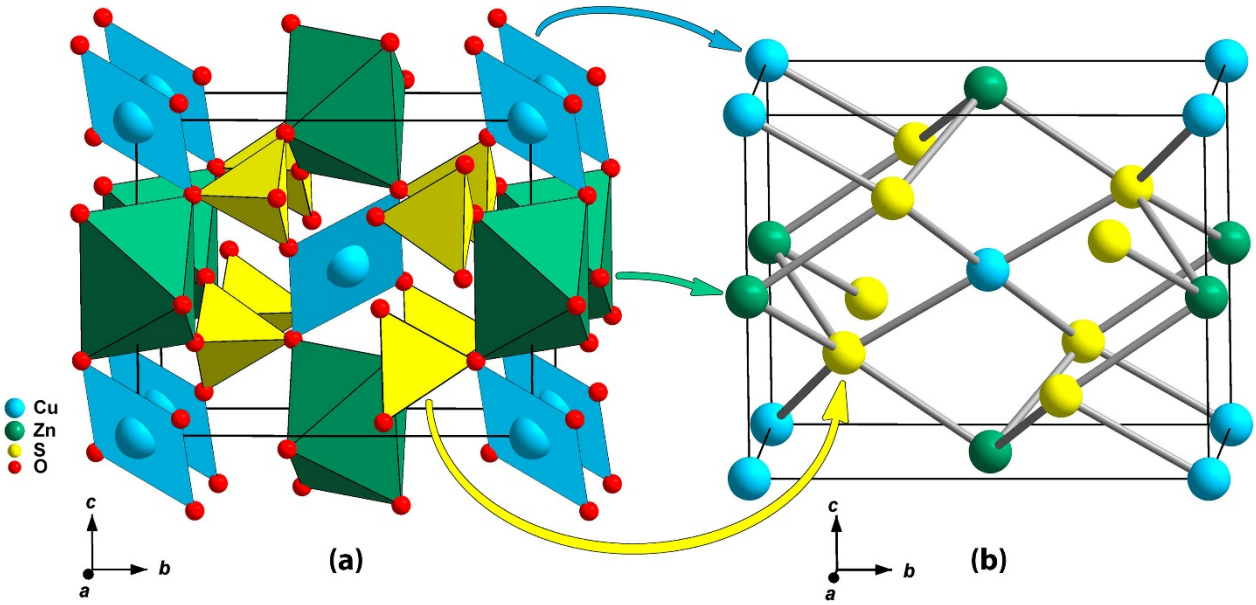

Figure 6. The standard simplification of hermannjahnite structure (***a***) into a periodic graph (net) (***b***).

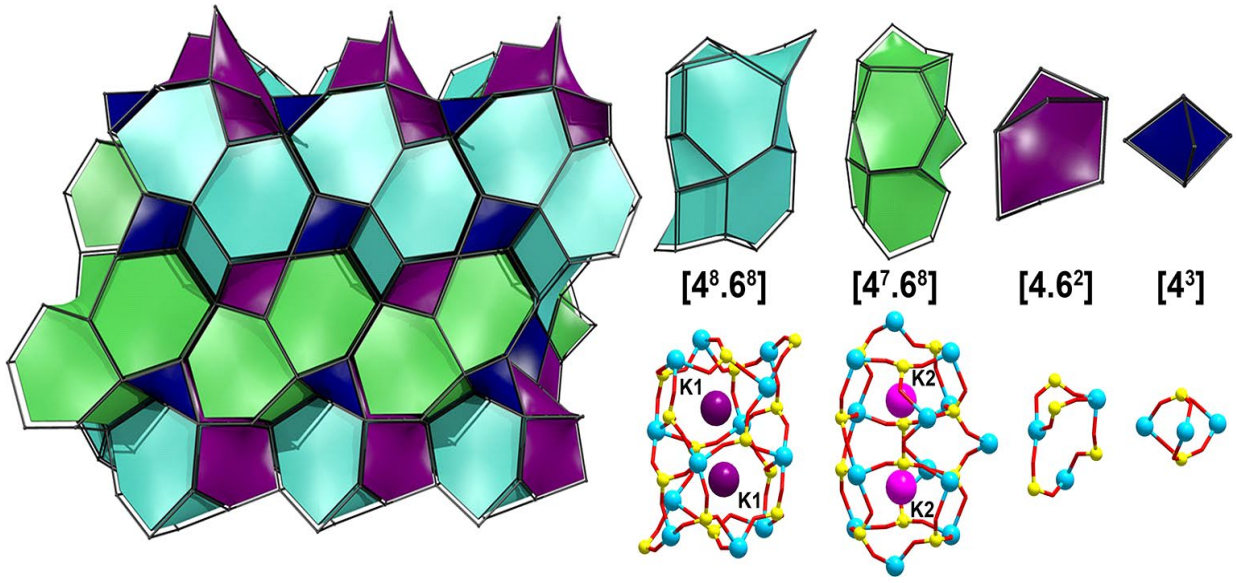

Figure 7. The natural tiling, tiles, and cages of the $K_2Cu_3(SO_4)_4$ structure.

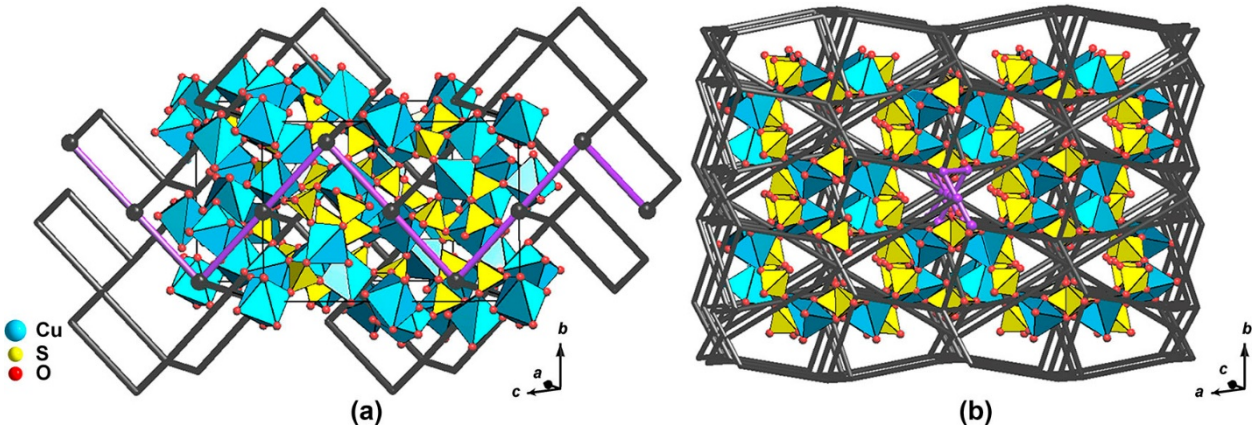

Figure 8. The 3*D* system of channels (rods) formed by the largest intra-framework cages of the $K_2Cu_3(SO_4)_4$ structure (***a***) and of the $KNaCu(SO_4)_2$ structure (***b***). The widest channels are highlighted by violet rods.

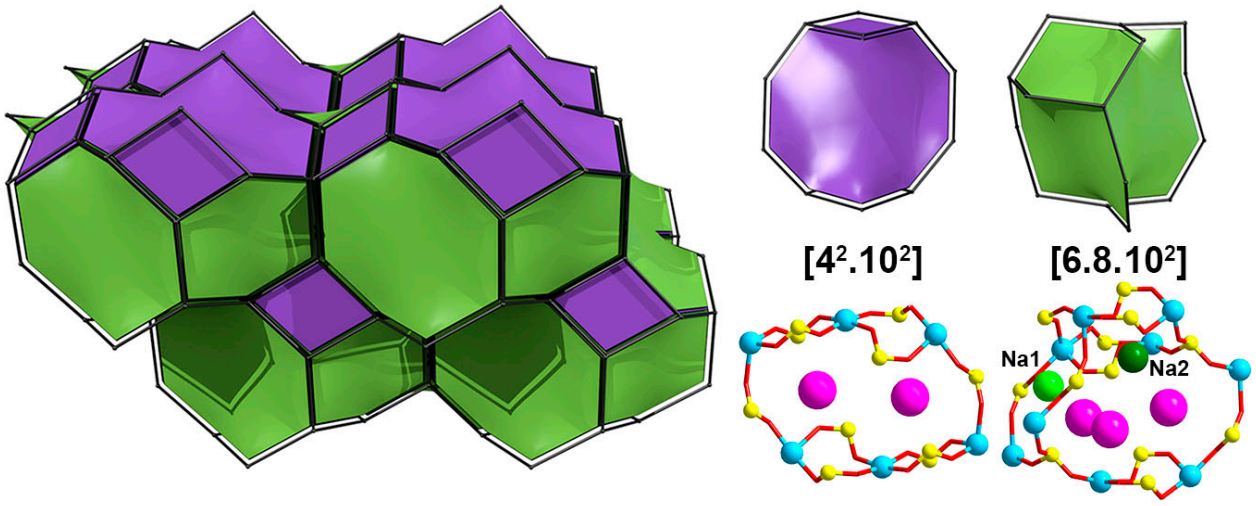

Figure 9. The natural tiling, tiles, and cages of the $KNaCu(SO_4)_2$ structure.

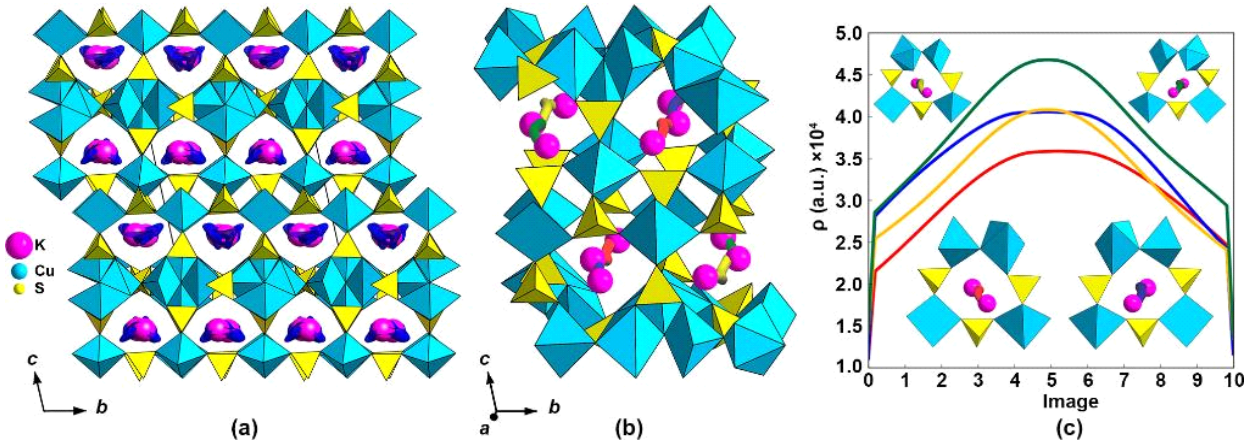

Figure 10. Transport conduction pathways of K^+ ions in cesiodymite, $CsK[Cu_5O(SO_4)_5]$, generated using the BVEL approach. The interconnected energy isosurfaces (royal blue color) along [100] plotted at 1.6 eV. Mixed populated (K, Cs, Rb) alkali metal cationic sites are shown by pink balls (***a***). Two symmetrically non-equivalent 1-periodic potential ion migration maps of $K_2[Cu_5O(SO_4)_5]$ running along [100]. These maps connecting pink-coloured K cationic sites consist of alternating red and blue or green and yellow pieces (***b***). The electron density profiles of these pieces calculated by the electron density approach, are shown together with their respective "bottlenecks" by the Cu-SO_4 - framework and arranged according to the maximum barrier along the respective path (***c***).

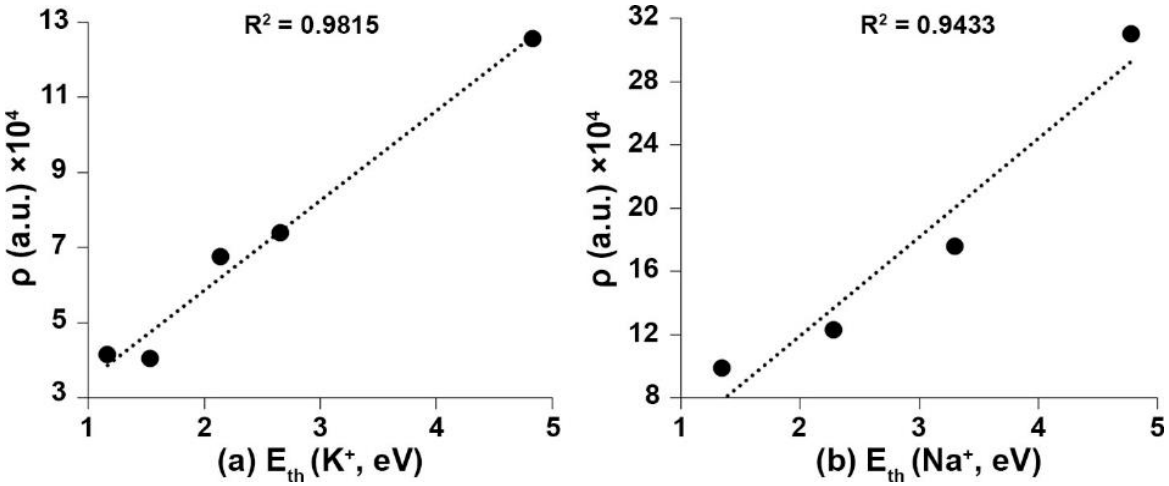

Figure 11. Maximal values of electron density (ρ) along the gradient paths that form a periodic map plotted against the threshold values of energy (E_{th}) calculated by BVEL for potassium (***a***) and sodium (***b***) containing compounds (*cf*. Tables 9, 10, 11), demonstrating good correlation.

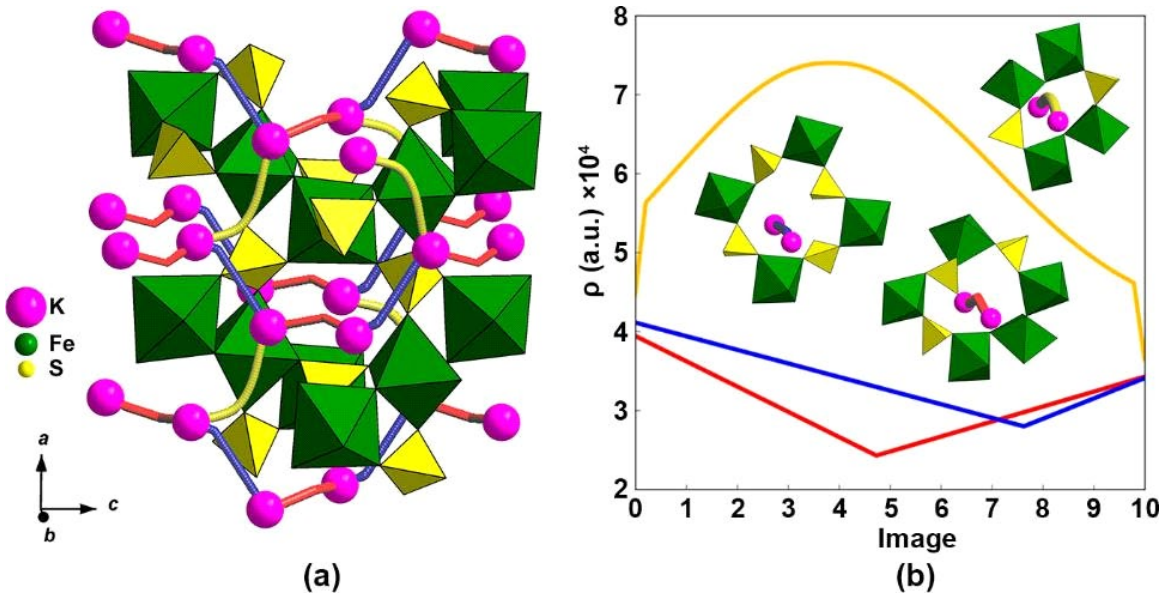

Figure 12. The lowest barrier 3-periodic ion migration map of K[$FeSO_4F$] (***a***) and the electron density profile (***b***) along structural "bottlenecks" as calculated by the electron density approach.

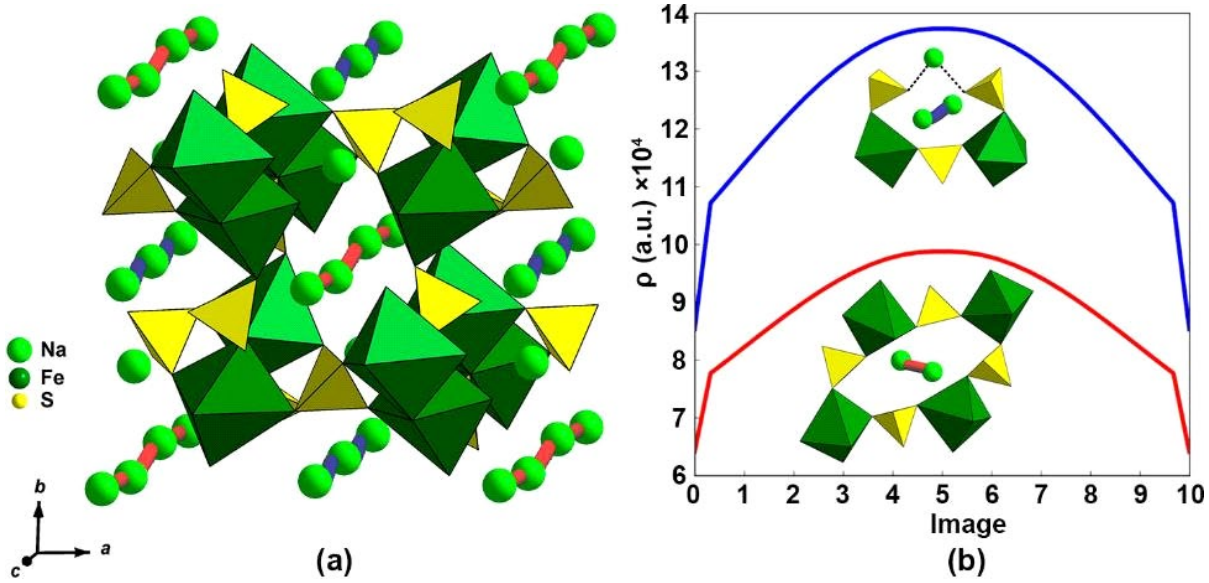

Figure 13. The 1-periodic ion migration map of $Na_{2.56}[Fe_{1.72}(SO_4)_3]$ (***a***) and the electron density profile (***b***) calculated by the electron density approach.